

Version 1.1 13 October 1996

To appear in *Astronomical Journal*

The I–Band Tully–Fisher Relation for Cluster Galaxies: Data Presentation

Riccardo Giovanelli, Martha P. Haynes, Terry Herter and Nicole P. Vogt

Center for Radiophysics and Space Research and National Astronomy and Ionosphere Center¹,
Cornell University, Ithaca, NY 14853

Gary Wegner

Dept. of Physics and Astronomy, Dartmouth College, Hanover, NH 03755

John J. Salzer

Astronomy Dept., Wesleyan University, Middletown, CT 06459

Luiz N. Da Costa

European Southern Observatory, Karl Schwarzschild Str. 2, D–85748 Garching b. München,
Germany

Wolfram Freudling

Space Telescope–European Coordinating Facility, Karl Schwarzschild Str. 2, D–85748 Garching b.
München, Germany

ABSTRACT

Observational parameters which can be used for redshift-independent distance determination using the Tully–Fisher (TF) technique are given for 782 spiral galaxies in the fields of 24 clusters or groups. I band photometry for the full sample was either obtained by us or compiled from published literature. Rotational velocities are derived either from 21 cm spectra or optical emission line long-slit spectra, and converted to a homogeneous scale. In addition to presenting the data, a discussion of the various sources of error on TF parameters is introduced, and the criteria for the assignment of membership to each cluster are given.

Subject headings: galaxies: distances and redshifts; photometry – cosmology: observations; cosmic microwave background

¹The National Astronomy and Ionosphere Center is operated by Cornell University under a cooperative agreement with the National Science Foundation.

1. Introduction

The observed radial velocity of a galaxy is

$$cz = H_0 d + [\mathbf{V}_{pec}(\mathbf{d}) - \mathbf{V}_{pec}(0)] \cdot (\mathbf{d}/d) \quad (1)$$

where \mathbf{V}_{pec} is the peculiar velocity vector, \mathbf{d} is the vector distance to the galaxy and d its modulus. The Tully–Fisher (TF) technique yields estimates of $H_0 d$ and cz can generally be obtained directly and with high accuracy from a galaxy’s spectrum. If the Cosmic Microwave Background (CMB) radiation dipole moment is interpreted as a Doppler shift resulting from the motion of the Local Group with respect to the comoving reference frame, $\mathbf{V}_{pec}(0)$ can be inferred from the CMB dipole and the peculiar velocity of the galaxy can be obtained from eqn. (1), independently on any assumption regarding the value of H_0 . In this paper we shall often refer to $H_0 d$ as “distance”, with the understanding that such quantity is intended expressed in km s^{-1} . The necessary ingredients in this operation are a set of photometric and spectroscopic data and a template TF relation, which is empirically derived.

Clusters of galaxies are favorite targets for applications of the TF technique of determining redshift-independent distances $H_0 d$ for two important reasons. First, a cluster provides a large number of objects located at a common distance, thereby allowing the determination of a TF relation slope which will be exempt from the vagaries that are introduced by an *a priori* unknown peculiar velocity field in a field galaxy sample. Clusters are thus well suited for the generation of a TF template relation. Second, the combination of independent distance estimates of several galaxies in a cluster provides a more accurate determination of the cluster distance: to the extent that N galaxies in a cluster can be considered to be at the same distance, the cluster distance can be found $\sim N^{1/2}$ times more accurately than as determined for a single galaxy. Well-sampled clusters and groups can thus provide “hard points” in a map of the large scale peculiar velocity field.

Seminal work in the determination of redshift-independent cluster distances was carried out in the 1980’s by Aaronson and co-workers (1983,1986,1989), using a version of the TF relation that utilized H band aperture photometry, an approach thought to minimize the amplitude of internal extinction corrections and therefore to reduce the scatter that determines the ultimate accuracy of the distance determination technique. More recently, it has become common practice to carry out surface photometry for TF work using I or R band CCD images. The sky background at those wavelengths is still relatively low (as compared to H and K bands), detectors have high efficiency and large fields of view, and data acquisition is relatively fast even with small aperture telescopes. The population dominating the light at I band is comprised of stars that are several Gyr old. Thus, disks are well outlined but of smoother appearance than as seen in blue portions of the visible spectrum, and their apparent inclinations to the line of sight can be more reliably determined. In addition, the processes operating in clusters that may alter the star formation rate

in galaxies will have a very retarded effect on the red and infrared light of disks; thus, smaller — if any — systematic differences are expected between the I and R TF relation of cluster and field galaxies (Pierce and Tully 1992). Recent CCD TF cluster work includes the surveys of Pierce and Tully (1988; hereafter PT88), Han (1992) Han and Mould (1992), hereafter jointly referred to as HM, Schommer *et al.* (1993), Mathewson *et al.* (1992; hereafter MFB) and Bernstein *et al.* (1994).

Published cluster samples suffer from a number of limitations:

- (i) Spirals are rare in the central parts of clusters and, when found there, are often gas deficient, especially in the outer disk where rotation curves tend to flatten. As a result, HI and optical emission line measurements of rotational speeds are scarce and difficult to obtain in cluster cores.
- (ii) High velocity resolution HI emission work, even for spirals of normal gas content, becomes arduous at redshifts larger than few thousand km s^{-1} with most radio telescopes, except for a few (Arecibo, Nançay) that are jointly unable to reach the whole sky. Thus galaxies with TF distance measurements tend to be the brightest in the cluster, and TF cluster samples mix optical and radio widths.
- (iii) In order to maximize sample size, cluster membership assignment has sometimes been made with relatively lax criteria: galaxies in TF cluster samples have tended to be representatives of an extended supercluster population rather than strict cluster members. As observations of increasing sensitivity are made and the data base of cluster galaxy TF distances grows, it becomes possible and desirable to apply stricter membership criteria, significantly improving the quality of the determination of both the parameters of the TF template relation and of the motions of individual clusters.

As a complement to a program to map the local peculiar velocity field via TF distance measures of approximately 2000 field spirals (Giovanelli *et al.* 1994, hereinafter Paper I, Giovanelli *et al.* 1995: Paper II, Freudling *et al.* 1995: Paper III, Giovanelli *et al.* 1996a: paper IV, da Costa *et al.* 1996: paper V), we present here the results of a TF survey restricted to cluster galaxies suitable both for the determination of a template TF relation and for the determination of the amplitude of the motions of the clusters themselves. Extending previous work, in this study we utilize a larger data base, strict membership criteria for the definition of cluster samples, as well as recent determinations of correction recipes for the observed TF parameters (Papers I and II). The data base presented here contains both new photometric and spectroscopic data for several hundred galaxies, and the results of the reprocessing of relevant data available in the public domain. The observational data are utilized to produce a TF template and to investigate cluster motions in a companion paper (Giovanelli *et al.* 1996b, hereinafter referred to as Paper VII).

In section 2, we discuss the cluster selection and the data sets used. In section 3, we present the individual galaxy parameters. In sections 4, 5 and 6 we discuss the procedures followed to derive disk inclinations, velocity widths and I band fluxes. The global properties of the cluster galaxy sample are investigated in section 7, while cluster membership assignment issues are

discussed in section 8.

Throughout this work, we parametrize distance dependent parameters by assuming a distance scale $H_0 = 100h \text{ km s}^{-1} \text{ Mpc}^{-1}$. Whenever explicit dependence on h is not made, a value of $h = 1$ is assumed.

2. The Selection of Clusters and Data Sets

In this section, we discuss alternative strategies for deriving the template relation and, in particular, the approach we have taken. Note that a template TF relation for the measurement of peculiar velocities requires an accurate estimation of a *velocity zero point*, which can be obtained independently on any assumption for, or knowledge of the value of the Hubble constant. Ideally, the objects entering the definition of the TF template will be globally at rest in the comoving reference frame, assumed to be the one where the CMB dipole moment vanishes.

While the use of local calibrators with reliable estimates of primary distances is necessary if the TF relation is used for the determination of the Hubble constant, it is of no consequence in defining a peculiar velocity TF template. Since only a handful of galaxies with primary distances exist, which can also be profitably used for TF work, they allow a determination of the TF zero point to no better than $\sim 0.1 \text{ mag}$. Note that a TF template relation with $\sim 0.1 \text{ mag}$ distance modulus predictive accuracy is clearly unsatisfactory for the measurement of the velocity field, as it would introduce large, spurious and systematic peculiar velocities of growing amplitude in the outer regions of any sampled volume.

2.1. Single Cluster Template

One commonly-adopted approach to the determination of a TF template relation is to select a single cluster of galaxies as a reference, thereby equating the universal template with the TF relation defined by its member galaxies (PT88; MFB). In this instance, all cluster members are assumed to be at approximately the same distance from the observer as predicted by the systemic velocity of the cluster, and their relative locations in the TF diagram are assumed to be unaffected by peculiar motions. This strategy requires that the cluster be endowed with several special qualities: (a) a substantial number of individual galaxy distances must be measurable for that cluster, either by virtue of its large spiral population or of its proximity; (b) there must be a reasonable expectation that the cluster is at rest in the comoving reference frame; (c) there must be strong reasons to believe that the cluster’s TF relation is a particularly good approximation to the true one. The practical advantages of having a TF relation defined by a large sample of objects, as required by (a), are obvious; the likelihood that a reliable template can be obtained from a *single* cluster is however questionable on statistical grounds.

Consider the case of a nearby cluster first. We assume that a cluster TF relation is a random realization of some universal relation, defined by a zero offset and a slope. Uncertainty is contributed by the limited accuracy of measurements, by an intrinsic amount of scatter in galaxies’ properties and by the *a priori* unknown amplitude of the cluster motion with respect to the comoving reference frame. If the number of observed galaxies is large and the dynamic range in the observed parameters high, then the slope of the universal relation should be increasingly well approximated by that of the chosen cluster. These requirements favor the selection of a nearby cluster in which the fainter galaxies are more easily observable. The uncertainty on the offset or zero point of the TF relation can also be initially reduced by increasing the size of the sample. However, the limit of this process depends on the amplitude of the cluster motion itself, and for a given amplitude, the introduced uncertainty increases with cluster proximity. In other words, if the chosen cluster is nearby, the TF zero point uncertainty remains very high, independent of the size of the sample. Note that the uncertainties on the TF zero point and slope are coupled quantities.

Consider now the case of a distant cluster, where the average single-point scatter about a best fit linear relation is on the order of a third of a magnitude. A typical TF cluster sample may include two dozen galaxies, so that the cluster zero offset can be determined to better than 0.1 mag. A cluster motion of 300 km s^{-1} — about half the velocity of the LG with respect to the CMB reference frame — translates into an offset of the cluster TF relation smaller than 0.1 mag only if the cluster is at $cz > 6000 \text{ km s}^{-1}$. There is no *a priori* validity to expecting that the desired quality (b) listed above may hold for any given cluster. If we were to use a single cluster as reference, we would then be forced to use a distant one, which would limit both the number and the dynamic range in luminosity of the sampled galaxies.

2.2. “Basket of Clusters” Template

A more attractive approach is that of building a template by combining data of many clusters. It is reasonable to expect that the mean motion of a “basket of clusters”, if well distributed over all the sky, approximates null velocity better than any single cluster. The TF relation parameters can be statistically better determined, as the larger number of objects sampled help to reduce statistical uncertainties. Nearby clusters in the set play an important role in the definition of the template slope, while the more distant clusters allow a fairer definition of the kinematical zero point. In order for the TF relation of each cluster to be adequately “spliced” to that of the others, it is necessary to ascertain its peculiar velocity with respect to the reference frame defined by the cluster set.

Convinced of the superiority of this approach, we have thus assembled TF data for 24 clusters of galaxies. In their majority, the data are new, and obtained by us at the observatories of Arecibo, Palomar, MDM, Kitt Peak, Cerro Tololo, Green Bank and Nançay. The raw data, details of the observing schedules and data reduction techniques will be given in separate papers. Here

we present the final parameters, in a stage ready for utilization in astrophysical applications.

2.3. Cluster Selection

The clusters are all relatively nearby; their systemic velocities, as measured in the CMB reference frame, are all less than $10,000 \text{ km s}^{-1}$. They span a large range in richness: the sample includes dynamically evolved structures such as the Coma cluster and loose groups such as MDL59. It should be admitted that an important criterion for selection was one of expediency, i.e. a group or cluster may have been included in the sample if high quality velocity widths and I band photometry were available for a substantial number of member galaxies. We have not used certain clusters or groups, which have appeared in other cluster lists, for a variety of reasons. If photometry was not available in the I band, and thus it could not be reprocessed according to the same precepts followed for our sample, we preferred to forego the uncertain task of cross-calibration of data of various optical bands. In few cases in which I band data was available, after our cluster membership criteria were applied the number of remaining galaxies with measured distances for the cluster or group was so small (or cluster definition so uncertain) that the structure did not constitute a worthwhile addition. For example, the cluster A534, for which a significant amount of data is available, including our own, is at very low galactic latitudes. Although the size of the data set and cluster definition would warrant its use, the very high uncertainty and clumpiness in the extinction arising within our Galaxy make the data set currently unfit for TF calibration use. A significant amount of data is also available for the Sculptor group. This is a nearby group, for which a Cepheid distance modulus of 26.5 ± 0.2 has been measured for one of its brightest members (NGC 300; Freedman *et al.* 1991); however, the group appears to be quite extended along the line of sight, perhaps as much as 2 mag in distance modulus (Pierce and Tully 1992). We have thus chosen to exclude it from our sample. The Virgo cluster, nearby and well studied, exhibits very significant substructure, and will be the object of a successive focused study by our group.

We were also guided by the second important criterion that the sample should be as balanced as possible between contributions from different parts of the sky. Spatial balance in the cluster sample is required so that the kinematical zero point of the TF template, the derivation of which we describe in Paper VII, will be as closely as possible consistent with null velocity with respect to the CMB. We have been partly succesful, although the more distant clusters in the sample are principally located in the Northern hemisphere. Three stereographic views of the distribution of the 24 clusters are presented in figure 1, where their locations are in Cartesian Supergalactic coordinates (X, Y, Z) , expressed in km s^{-1} as measured in the CMB reference frame (Kogut *et al.* 1993). The conversion of cluster centers and systemic velocities to (X, Y, Z) is done using the apex parameters as given in the RC3 (de Vaucouleurs *et al.* 1993), and it does not correct the coordinates for the clusters' peculiar velocities.

Table 1 lists the main parameters of the chosen clusters. Standard names are listed in column

1; in a few cases (NGC 383, NGC 507, NGC 3557), the group is identified by the name of the most prominent galaxy. Adopted coordinates of the cluster center are listed in columns 2 and 3, for the epoch 1950; they are in general obtained from the same sources yielding cluster redshifts, except in a few cases discussed in Section 8. The systemic velocities, heliocentric and within the CMB reference frame, are listed in cols. 4 and 5 respectively. An estimated error for the systemic velocity is given between brackets after the heliocentric figure. Sources for centers and systemic velocities are given in col. 11. Angular and Cartesian supergalactic coordinates are given in cols. 6 and 7, and in cols. 8–10, respectively. When a source for the cluster parameters is not given in Table 1, it should be assumed that we have rederived them using compilations of redshift data, which occasionally include a richer data set than used in the most recent published analyses of those groups or clusters. Available redshift data have also been used in the assignment of cluster membership to individual galaxies.

For the I band photometry, we adopt data from several sources. The main ones are: (a) our own survey of cluster and field objects, carried out using the MDM 1.3m and the Kitt Peak 0.9m telescopes (the raw data and the technical details of these observations will be presented elsewhere); (b) the data sets published by HM and (c) that of MFB. In the case of the Ursa Major cluster, we make extensive use of the data of PT88.

For the velocity width data, the main sources of observational material are: (a) our own 21 cm and optical rotation curve data obtained at several telescopes, namely Arecibo, Green Bank (both 300 foot and 140 foot telescopes), Nançay, Effelsberg and Palomar (the raw data and the technical details of these observations will be presented elsewhere); (b) the data set of MFB and of numerous other sources of 21 cm widths.

Observed raw parameters of all data sets have been reprocessed, converting them into a homogeneous sample, to which a consistent set of correction algorithms has been applied. Details of those corrections are given in sections 4 to 6.

3. Galaxy Data

In Table 2² we list parameters of individual galaxies for each cluster set. Data for a total of 782 galaxies are presented. Of those, 374 are classified as bona fide cluster members, and an additional 210 are “peripheral” cluster members as defined below. The remainder of 198 galaxies consists of either foreground or background field objects, or pertains to groups or clusters not used in the TF template analysis. Figures 2 through 12 display their spatial and velocity locations. For each cluster two plots are given: in the upper panel the distribution of objects in the sky is shown, while in the lower panel each galaxy’s radial velocity is plotted versus the angular distance from

²Table 2 is presented in its complete form in the AAS CD-ROM Series, volume 8, 1997. The first page of 23 is presented here for guidance regarding its form and content. Electronic copies can be obtained from the first author.

the cluster center. For each cluster field, galaxies with measured TF distances are separated into three main classes: (i) objects that, on the basis of positional and velocity data, can be assigned cluster membership (we refer to these as the **in** sample); they are generally identified by filled circles in figures 2 through 12; (ii) objects with velocities very close to the systemic velocity of the cluster but spatially removed from their center so that a firm membership assignment cannot be made; they are identified by unfilled circles in Figures 2 through 12 and will sometimes be referred to as “peripheral” cluster objects; the combination of these objects with those in the **in** sample will be said to form the **in+** sample; (iii) foreground and background galaxies are generally plotted using asterisks. In some of the cluster plots the object identification may be slightly more complicated, as for example when more than one cluster is included in a single figure: see then the relevant figure caption, the description of col. 7 in Table 2 below and the comments for individual clusters in Section 7. Galaxies with redshifts known to us but with no measured TF distance (i.e. lacking I band photometry or an accurate estimate of width) are plotted in Figures 2 through 12 as dots. In the upper panel of each figure, circles with radius of respectively 1 and 2 Abell radii are plotted as dashed lines. In the lower panel of each figure, a solid horizontal line identifies the adopted systemic velocity of the cluster. In a few cases of clusters with a very rich redshift data base, caustic lines computed for $\Omega = 0.3$ are plotted as solid curves: for them the assignment of objects to the **in** sample is extended farther from the center of the cluster than for other clusters.

Entries in Table 2 are sorted first by the Right Ascension of each cluster, and within each cluster sample by increasing galaxy Right Ascension. The listed parameters are:

Col 1: one or two identification names. If the galaxy is listed in the UGC catalog (Nilson 1973), the UGC number is listed first; if not, the first listing corresponds to our own internal coding number, which we maintain for easy reference in case readers may request additional information on the object. The second galaxy name is added with the following priority scheme: if the galaxy has an NGC or IC number, that coding is entered preferentially; if the galaxy is listed in the CGCG (Zwicky *et al.* 1968), that coding is listed with second priority, in the form: field number – ordinal number within the field; for southern galaxies, if an NGC or IC number is not available, the Lauberts (1982) catalog name is entered. If entries in those four catalogs are not available, a second name is not entered.

Cols. 2 and 3: Right Ascension and Declination in the 1950.0 epoch, as listed by the observers or available in our compilation, whichever has higher accuracy; typically, the listed positions have 15” accuracy, including those in Southern clusters as reported by MFB (most of the positions were conveyed by us to MFB ahead of their observations).

Col. 4: morphological type code in the RC3 scheme, where code 1 corresponds to Sa’s, code 3 to Sb’s, code 5 to Sc’s and so on. When the type code is followed by a “B”, the galaxy disk has an identifiable bar.

Col. 5: the galaxy radial velocity as measured in the CMB reference frame (Kogut *et al.* 1993); this value is obtained from the source for the radial velocity and velocity width data, as specified

in col. 16.

Col. 6: the angular distance θ in degrees from the center of each cluster. When the cluster consists of several subclumps, such as in Cancer, the distance is measured from the center of the main clump (clump A in Cancer; see Bothun *et al.* 1983). This parameter is the abscissa in the lower panel of Figures 2 through 12.

Col. 7: membership code. In most cases the code consists of one of 4 letters: *c*, *g*, *f*, *b*. Code *c* signifies that the galaxy is considered a *bona fide* cluster member (**in** sample). Code *g* means that the galaxy is sufficiently removed from the cluster center that cluster membership cannot be safely assigned; the galaxy is however in the periphery of the cluster, at roughly the same redshift and it is a nearby supercluster member (**in+** sample). Codes *f* and *b* identify respectively foreground and background galaxies; these will not be used in the construction of the cluster TF relation in any form. Criteria adopted to arrive at the membership assignment are discussed in greater detail in the section 8. In some clusters, additional codes had to be used, due to the complex nature of the structure. We describe those codes separately below.

In Cancer, the cluster has been recognized to be an assembly of clumps, dubbed A, B, C, D (Bothun *et al.* 1983). We use the criteria given in that reference to assign membership to each of the clumps, and used correspondingly capital letters A, B, C and D as membership identifiers. In the remainder of this paper, when mention is made to “Cancer cluster members”, we refer to members of clump A, the largest of the system. In Figure 5, members of the other clumps in the region are plotted as unfilled squares (D clump) and triangles (clumps B and C).

In Centaurus (A3526), Lucey *et al.* (1986 and references therein) recognized the existence of two structures superimposed along the line of sight, concentric in projection, with systemic velocities respectively near 3,000 km s⁻¹ and near 4,500 km s⁻¹, thus referred to as Cen30 and Cen45. We assign the *c* membership code to galaxies deemed to be part of Cen30, the low velocity cluster. We don’t use galaxies in Cen45 for the construction of the TF template. We list separately objects in Cen45 (labelled as “4” in the relevant section of table 2) with foreground and background objects. The distinction between Cen30 and Cen45 is uncertain, especially in regions close to the cluster center, where virial distortions produce mixing of the two velocity fields. In cases of greater uncertainty, we have assigned membership preferentially to Cen45, in order to keep the Cen30 sample as “clean” as possible. It is thus likely that some of the objects assigned to Cen45 are Cen30 members; they are thus footnoted. In the remainder of the paper, when A3526 cluster members are mentioned, we refer to members of the Cen30 concentration. In Figure 8, objects assigned to Cen45 are plotted as unfilled squares.

In the A3574 (Klemola 27) field, a smaller, low velocity dispersion group is also present, identified by Abell, Corwin and Olowin (1989) as S0753. Three objects in the field are identified as members of that group and labelled with the letter *s*. As with background and foreground objects, no further TF use is made of those three galaxies. In the sky plot of A3574 in Figure 9, a rich cluster is clearly discernible approximately 4° NW of the center of A3574: it is A1736, at a

redshift $z \sim 0.04$.

Clusters A2197 and A2199, which are quite close in the sky, are listed jointly, so that peripheral galaxies, i.e. those of code g , are assigned to the binary cluster system rather than to either one of the two; angular distances θ for these objects are referred to the center of A2199. Members of A2197 are identified by a “7” and members of A2199 are identified by a “9”.

The case of A2634 (near $cz_{cmb} \sim 8900 \text{ km s}^{-1}$) and A2666 (near $cz_{cmb} \sim 7800 \text{ km s}^{-1}$) is the most complicated. Scodreggio *et al.* (1995) have produced a detailed study of the region, and within the redshift range spanned by the two clusters they also distinguished several other groups. In particular, one of the groups is at a systemic velocity near $7,000 \text{ km s}^{-1}$, near in redshift to, but distinct from A2666. We reserve the code “4” for the *bona fide* members of A2634, a code “6” for the members of A2666, and the code “7” for the members of the $7,000 \text{ km s}^{-1}$ group projected on the foreground of A2634. The code $g4$ is reserved for peripheral members of A2634 and $g6$ for the one peripheral member of A2666.

Col. 8: the measured velocity width, as reported by the source (see comments to col. 16 for details), in km s^{-1} . Radio widths refer to values measured at a level of 50% of the profile horns.

Col. 9: the velocity width in km s^{-1} after all corrections except that for inclination are applied; these corrections, including those for instrumental and data processing broadening, signal to noise effects, interstellar medium turbulence, shape of the rotation curve and cosmological stretch, are discussed in section 5.

Col. 10: the corrected velocity width converted to edge-on viewing, in km s^{-1} .

Col. 11: the adopted inclination i of the plane of the disk to the line of sight, in degrees, (90° corresponding to edge-on perspective); the derivation of i and its associated uncertainty are discussed in section 4.

Col. 12: the logarithm in base 10 of the corrected velocity width (value in col. 10), together with its estimated uncertainty between brackets. The uncertainty takes into account both measurement errors and uncertainties arising from the corrections. The format 2.228(11), for example, is equivalent to 2.228 ± 0.011 .

Col. 13: the measured I band magnitude, extrapolated to infinity assuming that the surface brightness profile of the disk is well described by an exponential function; this value is sometimes adopted as an average of two or more measurements, as footnoted.

Col 14: the apparent magnitude, to which k-term, galactic and internal extinction corrections were applied; details on the adopted corrections are given in section 6.

Col. 15: the absolute magnitude, computed assuming that the galaxy is at the distance indicated either by the cluster redshift, if the galaxy is a cluster member (**in** sample), or by the galaxy redshift if not. The calculation assumes $H_0 = 100h \text{ km s}^{-1} \text{ Mpc}^{-1}$, so the value listed in column 15 is strictly $M_{cor} + 5 \log h$. In calculating this parameter, radial velocities are expressed in the

CMB frame and uncorrected for any cluster peculiar motion. The uncertainty on the magnitude, indicated between brackets in hundredths of a mag, is the sum in quadrature of the measurement errors and the estimate of the uncertainty in the corrections applied to the measured parameter, as described in section 6. The error estimate does not include the uncertainty on the value of the distance.

Col. 16: Finally, references are given for the sources of the data and cautionary notes for individual objects. A letter code identifies the source for the photometry, as follows:

- a* refers to our own photometric observations;
- b* refers to photometric observations of Bernstein *et al.* (1994), restricted to Coma;
- h* refers to photometric observations reported by HM;
- m* refers to photometric observations of MFB;
- p* refers to photometric observations of PT88, restricted to Ursa Major;
- s* refers to photometric observations of Bureau *et al.* (1996; BMS), restricted to Fornax;
- x* refers to a combination of different sources, as noted.

A numerical code identifies the source for the velocity width:

- 0 refers to our own 21 cm measurements;
- 1 refers to our own optical spectroscopy;
- 2 refers to averages of several measurements; see notes in each case;
- 3 refers to 21 cm observations of Gavazzi (1987) and Scodeggio and Gavazzi (1993);
- 4 refers to 21 cm observations of Bothun *et al.* (1985), Aaronson *et al.* (1989), cross-referenced with the compilation of Bottinelli *et al.* (1990);
- 5 refers to 21 cm measurements of MFB;
- 6 refers to optical spectroscopy of MFB;
- 7 refers to 21 cm measurements reported by PT88;
- 8 refers to 21 cm observations of Fontanelli (1983), Lewis (1985) and Schneider *et al.* (1991);
- 9 refers to 21 cm observations of Bureau *et al.* (1996).

When an asterisk appears at the end of the record, a detailed comment is given for that particular object. Because of the length and number of these comments, they are not appended to the table but included in the text as follows. When two parameters are given in the notes for a given source, e.g. “HM (13.79,78)”, the first number refers to the raw magnitude and second to the disk inclination.

N383 Group:

453: tiny disk; exponential disk over narrow range of radii; photometric parms. uncertain.

100561: v. uncertain ellipticity.

557: 21cm line disturbed: comp. superimposed; galaxy not used for fits.

556: 21cm line disturbed: comp. superimposed? galaxy not used for fits.

565: discrepancy between HM (13.79,78) and us (13.72,75): use (13.75,75).

575: discrepancy between HM (13.77,90) and us (13.87,84): use (13.82,84).

629: note low i; not used in fits.

632: marginal 21cm spectrum.

633: discrepancy between HM (12.94,80) and us (13.02,80): use (12.98,80).

673: discrepancy between HM (14.25,71) and us (13.86,70): use (14.06,70).

697: marginal 21cm spectrum.

724: note low i.

110090: tiny disk; exponential disk over narrow range of radii; photometric parms. uncertain.

N507 Group:

800: note low i.

809: discrepancy between HM (13.59,90) and us (13.50,83): use (13.55,83).

810: discrepancy between HM (13.11,79) and us (13.04,78): use (13.07,78).

1013: discrepancy between HM (11.09,74) and us (11.20,72): use (11.15,73).

110334: tiny disk; exponential disk over narrow range of radii; photometric parms. uncertain.

110363: tiny disk; exponential disk over narrow range of radii; photometric parms. uncertain.

1094: discrepancy between HM (11.91,80) and us (12.01,79): use (11.96,80).

A262:

110463: tiny disk; exponential disk over narrow range of radii; photometric parms. uncertain, ellipticity may be underestimated.

1234: discrepancy between HM (13.63,51) and us (13.50,64) is large; not sure we were measuring same galaxy; use our parms.

1307: discrepancy between HM (12.07,81) and us (12.29,79): use (12.18,80).

1316: unclear ID of these I band data: U1316 or 522-023? assign to U1316 but caution.

1376: i uncertain; inner parts affected by bar asym., suggest high i; outer isophotes much lower i; adopt low i of outer.

1405: wiggly photometric profile; total magnitude quite uncertain.

1416: galaxy is 1.5 mag off mean TF relation: misident? not used in fits.

1456: large uncertainty on i affects mostly width.

1729: tiny disk; exponential disk over narrow range of radii; photometric parms. uncertain; unstable ellipticity.

A400:

2336: severe TF outlier; not used in fits.

2364: marginal membership assignment.

2367: Type S0a: uncertainty in corrections large.

2375: discrepancy between HM (12.93,76) and ours (13.17,81): use (13.05,79).

2405: discrepancy between HM (12.97,72) and ours (13.08,70): use (13.03,70).

2454: discrepancy between HM (13.87,85) and ours (13.89,79): use (13.88,80).

Eridanus:

22364: note low i ; not used in fits.

22413: note low i ; MFB give $i=49$, but their major and minor axis data yield $i=42$; we adopt $i=45$.

22472: note low i ; MFB give $i=49$, but their major and minor axis data yield $i=39$; we adopt $i=44$.

22479: width v . small: low reliability.

22625: width v . small: low reliability.

22735: width v . small: low reliability.

430438: discrepancy between MFB (11.67,89) and us (11.75,90): use (11.71,90)

430459: discrepancy between MFB (11.75,75) and us (11.62,73): use (11.68,73)

23183: width v . small: low reliability.

23560: width v . small: low reliability.

Fornax:

22003: note low i ; unreliable width; not used in fits.

22216: width v . small: low reliability.

22370: width v . small: low reliability.

22382: width very uncertain; measured on paper plot.

22447: discrepancy between BMS (12.46,52) and MFB (12.69,46): use (12.55,50).

22474: discrepancy between BMS (13.15,84) and MFB (13.17,79): use (13.16,82).

22502: note low i ; unreliable width: not used in fits.

22535: 21 cm profile inadequate for TF use: not used in fits.

22618: discrepancy between BMS (12.37,90) and MFB (12.16,79); use (12.26,86); 21 cm widths of BMS and MFB respectively 210 and 201: adopt 205.

22662: note low i ; also small, unreliable width: not used in fits.

22686: width v . small: low reliability.

22699: discrepancy between BMS (8.31,44) and MFB (8.40,47): use (8.35,46).

22820: discrepancy between BMS (10.65,90) and MFB (10.51,77): use (10.58,86).

22835: width v . small: low reliability.

22863: 21cm spectrum is poor; width v . small: v . low reliability.

22873: discrepancy between BMS (9.82,66) and MFB (9.74,63): use (9.78,65).

22924: width v . small: low reliability; cluster membership doubtful.

22934: width v . small, 21cm profile asymm: low reliability.

22940: discrepancy between BMS (10.71,84) and MFB (10.64,83): use (10.67,83).

23010: width v. small: low reliability.

23038: 21 cm widths of BMS and MFB respectively 173 and 179: adopt 175.

23099: width too small and poor opt. rot. curve; unreliable: not used in fits.

23806: MFB give $i=39$, but their axial ratio yields $i=46$; we adopt $i=43$.

Cancer:

4264: large galaxy, resolved by Arecibo beam; width (central beam only) uncertain; severe TF outlier: not used in fits.

180141: discrepancy between HM (14.07,90) and us (13.86,86): use (13.96,86).

180192: note low inclination: not used in fits.

180201: Han reports type Scd, but it may as early as S0a.

4344: note low inclination: not used in fits.

180631: tiny disk, with nonexponential profile; photometric parms. highly uncertain.

4354: discrepancy between HM (13.41,54) and us (13.65,59): use (13.53,57).

4361: discrepancy between HM (14.00,74) and us (14.12,74): use (14.06,74).

4375: Photometry v. uncertain: strongly affected by nearby stars in field.

4400: discrepancy between HM (14.56,89) and us (14.91,82): use (14.73,83).

4399: discrepancy between HM (13.64,70) and us (13.75,71): use (13.70,71).

180270: HI spectrum very likely blend with 119-094 at 1.5'.

4591: 21cm spectrum is blend: inaccurate extraction of width.

4595: 21cm spectrum is poor: inaccurate extraction of width.

Antlia:

26733: discrepancy between MFB (12.65,89) and ours (12.56,83): use (12.60,83).

26748: discrepancy between MFB (11.85,88) and ours (12.04,81): use (11.95,83).

26824: discrepancy between MFB (11.07,51) and ours (10.94,44): use (11.01,48).

26943: discrepancy between MFB (12.77,56) and HM (12.57,59): use (12.66,57).

26979: discrepancy between MFB (12.42,66) and HM (12.50,69): use (12.46,68).

26999: discrepancy between MFB (10.79,63) and HM (10.59,69): use (10.70,66).

27113: note v. low i ; unreliable width: not used in fits.

27146: our radial velocity ($v_{hel}=3899$) very discrepant from that of MFB ($v_{hel}=2946$); we adopt our velocity and width. Galaxy has LSB companion 3' NE: possibility of blend, affecting width, cannot be excluded.

27345: discrepancy between MFB (11.35,67) and HM (11.50,90), note inclination diff.; use (11.42,75), with large uncertainty.

27358: discrepancy between MFB (10.98,59) and ours (10.88,56); use (10.94,58).

27427: discrepancy between MFB (11.51,73) and HM (11.67,78); use (11.59,75). Large discrepancy in widths between MFB and HM: adopt corrected width of 331 ± 26 .

27462: discrepancy among MFB (11.89,80), HM (11.95,81) and us (11.82,78): use (11.88,78).

27475: discrepancy between MFB (10.28,72) and ours (10.22,68): use (10.25,69).

27495: discrepancy between MFB (11.33,81) and HM (11.49,90): use (11.41,84).

27501: discrepancy between MFB (12.16,50) and HM (12.18,52): use (12.17,51).

27580: discrepancy between MFB (10.69,72) and HM (10.75,71): use (10.72,71).

A1060 (Hydra):

26740: discrepancy between MFB (12.64,83) and us (12.33,78): use (12.48,79).

27187: discrepancy between MFB (13.18,59) and us (12.96,59): use (13.07,58).

27374: discrepancy between MFB (13.23,70) and HM (13.31,81): use (13.29,76): vel discrepancy of 300 km/s!

27404: discrepancy among MFB (12.48,75), HM (12.40,74) and us (12.14,70): use (12.33,72).

27407: discrepancy among MFB (13.45,52), HM (13.17,55) and us (13.38,54): use (13.34,54).

27419: severe TF outlier; possible misident.: not used in fit.

27441: discrepancy between MFB (11.77,61) and us (11.67,61): use (11.72,61). MFB velocity (4718) in disagreement with RC3 (5190) and ours (5243); use ours. Marginal membership in cluster.

27489: discrepancy among MFB (13.78,90), HM (13.79,90) and us (13.88,78): use (13.82,84).

27491: discrepancy between MFB (12.19,63), HM (12.07,65): use (12.13,64).

27529: note low i.

27584: our opt. parms agree with those of MFB (avg parms listed), but MFB’s rotation curve very poorly samples the optical disk, so width is severely underestimated. Not used in fits.

27598: discrepancy between MFB (11.96,60) and HM (11.95,66): use (11.95,63).

N3557 Group:

27705: discrepancy between MFB (11.41,80) and us (11.50,72): use (11.46,73).

27752: discrepancy between MFB (11.24,70) and HM (11.35,78): use (11.30,74).

27755: discrepancy between MFB (12.21,69) and HM (12.25,69): use (12.23,69).

27756: undetected by our 140’ telescope observations, which did not confirm Aaronson *et al.* (1989) Parkes detection: spurious? Not used in fits.

27803: discrepancy between MFB (12.11,57) and HM (12.19,64): use (12.15,60).

27829: v. large discrepancy between MFB (12.02,47) and HM (11.08,48): use (11.55,47).

27907: discrepancy between MFB (12.07,61) and HM (12.15,62): use (12.11,61).

27957: discrepancy between MFB (13.29,81) and HM (13.48,85): use (13.37,83).

A1367:

6525: nearly face on; inclination unreliable: not used in fits.

210482: uncertain morphology: bright offset nucleus, disturbed?

6583: 21cm spectrum blend, but width recovered.

210559: low S/N 21cm data; large uncertainty on width.

210612: poor 21cm data; uncertainty on width large.

6693: nearly face on; inclination uncertain: not used in fits.

6702: discrepancy between HM (12.53,36) and us (12.69,40): use (12.61,40); note low inclination.
210791: discrepancy between HM (13.26,71) and us (13.12,75): use (13.18,73).
210829: comp. within 2.2'; 21cm profile possibly confused.
210833: 21cm profile may be blended; low quality width.
6822: nearly face on; inclination uncertain: not used in fits.
210859: width derived from measurement at 20% of peak of Bothun *et al.* (1985).
6876: width unreliable; possibly blend: not used in fits.
210901: HM give mags at $23.5 \text{ mag arcsec}^{-2}$ isophote and total which are in great disagreement; we assume the former is correct, apply an avg. correction to total, and assign large uncertainty.

Ursa Major:

6802: uncertain mag.

Cen30:

28431: asymm. 21cm line profile; w50 prob. underestimates width, use w20.
28512: MFB's optical rotation curve samples small fraction of optical disk; width unreliable; not used in fits.
28657: discrepancy between MFB (11.97,52) and us (11.94,51): use (11.95,51).
28661: discrepancy between MFB (11.40,51) and us (11.35,53): use (11.37,52).
28708: discrepancy among MFB (10.30,51), HM (10.26,52) and us (10.23,53): use (10.26,52).
28756: discrepancy between MFB (13.83,83) and HM (13.73,86): use (13.78,81).
28820: discrepancy among MFB (13.68,75), HM (13.71,77) and us (13.75,75): use (13.71,75).
28832: discrepancy between MFB (12.68,60) and HM (12.68,64): use (12.68,60).
28928: discrepancy between MFB (11.67,60) and HM (11.61,59): use (11.64,59).
29086: discrepancy between MFB (13.87,67) and HM (13.78,74): use (13.82,70).
29188: discrepancy between MFB (13.40,69) and HM (13.29,68): use (13.37,69).
29277: width underest. by w50; use w=140.
29280: discrepancy between MFB (14.68,86) and HM (14.55,90): use (14.61,85).
29455: very low galactic latitude; galactic extinction exceeds 0.35 mag.

Cen45, background and foreground of Cen30:

28442: discrepancy between MFB (10.34,72) and HM (10.66,75): use (10.50,73).
28467: discrepancy between HM (11.99,68) and MFB (12.17,68): use (12.08,68).
28696: discrepancy between MFB (13.38,79) and HM (13.59,81): use (13.48,79); may be Cen30 member.
28774: discrepancy between MFB (12.58,53) and HM (12.68,60): use (12.62,57).
28923: discrepancy between MFB (11.69,59) and us (11.74,56): use (11.72,57).
28979: discrepancy between MFB (12.20,75) and HM (12.34,72): use (12.27,72); may be Cen30 member.
29033: very low galactic latitude (13°); large (0.51 mag), highly uncertain galactic extinction correction.

29151: low galactic latitude; galactic extinction exceeds 0.4 mags.

29153: low galactic latitude; galactic extinction exceeds 0.4 mags.

29181: discrepancy between MFB (12.71,43) and HM (12.83,55): use (12.76,49).

29351: discrepancy among MFB (11.80,87), HM (11.64,85) and us (11.80,80): use (11.75,82).

A1656 (Coma):

7845: discrepancy between B94 (14.07,76) and us (13.91,78): use (13.99,78).

7955: discrepancy between B94 (13.42,83) and us (13.49,83): use (13.46,83).

221022: 21cm profile has wide pedestal; width quite uncertain: could be as wide as 375 or as narrow as 230.

7978: discrepancy between B94 (13.21,52) and us (13.15,55): use (13.18,53).

8013: discrepancy between B94 (13.75,77) and us (13.64,79): use (13.69,78).

8017: discrepancy between B94 (12.52,77) and us (12.62,73): use (12.57,75).

221149: poor quality optical rotation curve.

8082: image has very poor seeing; inclination v. uncertain.

8096: discrepancy between HM (13.28,87) and us (13.11,90): use (13.20,88).

8161: discrepancy among HM (13.19,64), B94 (13.14,65) and us (13.11,64): use (13.14,64).

230051: marginal member, on caustic.

8220: discrepancy between B94 (12.65,82) and us (12.74,85): use (12.70,83).

8244: discrepancy between B94 (14.09,70) and us (14.16,70): use (14.13,70).

ESO508:

29076: discrepancy between MFB (12.02,73) and HM (11.72,76): use (11.87,73).

29082: discrepancy among MFB (12.67,89), HM (12.74,90) and us (12.71,85): use (12.69,86).

29140: discrepancy among MFB (12.35,39), HM (12.23,48) and us (12.32,39): use (12.30,40).

29175: discrepancy between MFB (11.75,90) and HM (11.83,90): use (11.78,88).

29216: discrepancy between MFB (13.04,77) and HM (13.16,78): use (13.09,76).

29264: discrepancy among MFB (12.61,90), HM (12.59,90) and us (12.52,84): use (12.56,84).

29307: discrepancy among MFB (12.86,71), HM (12.89,80) and us (12.97,69): use (12.91,70).

29327: discrepancy between MFB (12.71,70) and us (12.56,69): use (12.62,69).

29332: Note low i ; width unreliable.

530053: discrepancy between MFB (11.09,75) and us (11.13,77): use (11.11,76).

29361: discrepancy among MFB (12.16,90), HM (12.19,90) and us (12.21,82): use (12.19,83).

29371: discrepancy among MFB (11.62,84), HM (11.72,90) and us (11.65,81): use (11.66,82).

29453: discrepancy between MFB (13.69,86) and us (13.73,83): use (13.71,83).

29486: discrepancy among MFB (11.50,47), HM (11.48,42) and us (11.44,44): use (11.47,44); Aaronson *et al.* (1989) at $V_{hel}=3066$ disagree with MFB and Dressler (1991): velocity of Aaronson *et al.* probably spurious.

29501: discrepancy between MFB (13.48,58) and HM (13.29,62): use (13.39,60).

29511: discrepancy among MFB (12.80,88), HM (13.20,83) and us (12.72,78): use (12.90,80).

29585: discrepancy among MFB (11.31,47), HM (11.33,47) and us (11.32,47): use (11.32,47).

29608: feature in MFB 21cm spectrum, judged by them to be interference, may be part of signal; width v. uncertain and prob. underestimated.

A3574 (Klemola 27):

29565: discrepancy between MFB (14.14,90) and us (14.16,87): use (14.15,88).

29708: discrepancy between MFB (10.53,74) and HM (10.36,75): use (10.45,73).

29737: discrepancy between MFB (13.53,74) and us (13.39,72): use (13.46,72).

29872: discrepancy between MFB (11.72,83) and us (11.77,80): use (11.75,81).

29909: discrepancy between MFB (12.72,64) and HM (12.74,64): use (12.73,64).

30065: discrepancy between MFB (13.17,90) and HM (13.20,90): use (13.18,84).

30158: discrepancy among MFB (12.03,59), HM (11.93,63) and us (12.12,70): use (12.03,64).

30307: discrepancy between MFB (11.59,51) and HM (11.34,45): use (11.47,48); note v. low and prob. underest. width. TF outlier by nearly 2 mags; not used in fits.

30425: discrepancy between MFB (12.64,90) and us (12.68,87): use (12.65,87).

A2197/A2199:

260481: marginal cluster membership.

10389: marginal cluster membership.

260543: very unstable isophotal ellipticity: outer isophotes have $i=57$, inner $i=75$; uncertainty in parms. from poorly constrained i .

260561: note low i : not used in fits.

260622, 10417, 10423, 260640: images taken in very poor seeing; i v. uncertain.

S0805 (Pavo 2):

31805: very limited sampling of the optical disk; width v. uncertain; not used for fits.

31871: large discrepancy between MFB optical and MFB radio widths; both spectra of good quality; use avg.

31969: note low i . Rotation samples very poorly optical disk; width v. uncertain; not used in fits.

32003: large discrepancy between MFB optical and MFB radio widths and velocities: “noise” feature in 21cm line probably part of signal; use W_{opt} , even if also poor.

32005: note low i ; inadequate for TF use; not used in fits.

32068: MFB’s rotation curve asymm, reaches $60''$ on one side, $20''$ on other: width and vel v. uncertain.

32175: note significant discrepancy between MFB 21cm and optical widths; both appear of good quality: use avg.

32709: Rotation curve samples v. poorly the optical disk; width v. uncertain; not used in fits.

MDL59:

34434: low S/N, Gaussian-shaped 21cm spectrum; use $w_{20}=220 \text{ km s}^{-1}$.

34682: discrepancy between MFB (12.37,77) and us (12.04,82): use (12.19,80).

34685: 21cm spectrum of MFB poor; w20 appears better representation of $2 \times V_{\text{rot}}$ than w50.

34852: note low i . Inadequate for TF use; not used in fits.

34875: note low i . Inadequate for TF use; not used in fits.

34977: discrepancy between MFB (13.59,77) and us (13.86,78): use (13.72,78).

34989: note width small and uncertain.

35083: 21cm spectrum poor; after inspection, use W21=166 as better representation of width than 146.

35331: discrepancy between MFB (14.47,76) and us (14.31,73): use (14.39,73).

35781: note low inclination; not used for fits.

Pegasus:

12382: discrepancy among HM (14.43,90), MFB (14.37,81) and us (14.40,80): use (14.40,80); TF outlier by 1.5 mag: not used in fits.

12417: discrepancy among HM (14.03,67), MFB (12.76,61) and us (12.72,62); prob. misidentification by HM: use (12.72,62).

12423: discrepancy among HM (12.39,90), MFB (12.57,90) and us (12.30,81): use (12.40,83).

12437: discrepancy between HM (12.24,66) and MFB (12.37,65): use (12.30,65).

12467: discrepancy between HM (13.30,79) and MFB (13.75,81): use (13.52,79).

12483: discrepancy between HM (12.66,50) and MFB (12.76,57): use (12.71,54).

12494: discrepancy between HM (13.68,74) and us (13.93,77): use (13.80,76); also note that 12494 is in double system.

12498: discrepancy between HM (12.37,62) and us (12.63,62): use (12.50,62).

330261: i highly uncertain: not used in fits.

12555: discrepancy among HM (14.46,79), MFB (14.75,78) and us (14.75,77): use (14.65,77).

12561: discrepancy between HM (13.92,77) and MFB (14.41,75): use (14.16,75).

A2634/A2666:

330564: marginal cluster membership assignment.

331234: in probable interacting system: cautionary TF use.

330663: poor (S/N) on spectrum; v . uncertain width.

12721: discrepancy between HM (13.01,63) and us (12.76,65): use (12.89,64).

4. Inclinations

For galaxies for which we had available access to the I band images, inclinations were obtained after fitting ellipses to isophotal contours using the ISOPHOTE routine in STSDAS, as described in paper I. From these isophotal fits, one can obtain an ellipticity — defined as $e = 1 - b/a$, where a and b are the major and minor axes of the ellipse — as a function of the distance $r = a/2$ from the center of the galaxy. A range of radial distances is then chosen over which the disk appears to be exponential, and a mean value of the ellipticity \bar{e} is obtained. This parameter yields a

first order approximation to the true ellipticity of the image, which needs to be corrected for the effects of resolution, mainly the smearing effects of seeing. We assume that the disk light drops to half power near $a' = 0.2a_{23.5}$ and $b' = 0.2b_{23.5} = 0.2a_{23.5}(1 - \bar{e})$ respectively along the major and minor axes, where $a_{23.5}$ and $b_{23.5}$ are the major and minor isophotal sizes at the 23.5 I mag sec^{-2} isophote; this results from the fact that, statistically, $a_{23.5}$ is about equal to 3.5 scale lengths. Then if $\psi = 0.5\text{HPFW}_{\text{seeing}}/a'$, where $\text{HPFW}_{\text{seeing}}$ is the size of the seeing disk for the given observation, we adopt as the corrected ellipticity

$$e_{\text{corr}} = 1 - \sqrt{\frac{(1 - \bar{e})^2 - \psi^2}{1 - \psi^2}} \quad (2)$$

In order to avoid overcorrection, we limit e_{corr} to not exceed a maximum value of $(0.12)^{-1}$, and assume e_{corr} is a good approximation of the true value of e . In the following, when we refer to e , we mean the corrected value given by eqn. (2), unless otherwise specified.

The inclination angle is then derived as

$$\cos^2 i = \frac{(1 - e_{\text{corr}})^2 - q_o^2}{1 - q_o^2} \quad (3)$$

where q_o is the intrinsic axial ratio of spiral disks, which are treated as highly oblate spheroids. For Sbc and Sc galaxies, we adopt $q_o = 0.13$, as discussed in paper I; for other types we adopt a more conservative $q_o = 0.2$.

In the published literature, inclinations have occasionally been obtained using criteria different from our own. Both MFB and HM, for example, adopt an intrinsic disk axial ratio of 0.2 for all types. In those cases, we rederive an axial ratio from the published inclination, and use it to estimate the inclination according to our choice of intrinsic axial ratio q_o . A problem with this approach is that published inclinations obtained using $q_o = 0.2$ yield values of e that saturate at 0.80; for a $q_o = 0.13$, that ellipticity yields an inclination of 81° . In the case of MFB, in addition to inclinations also axial ratios are given, so that the ambiguity can be partially solved: whenever their published inclination is 90° (which would yield 81° for a $q_o = 0.13$), we recompute the ellipticity from their reported axial ratio, and use it to estimate the inclination, with the value of q_o appropriate to our convention. In the case of HM's data, axial ratios are not available, and inclinations reported at 90° are kept at that value, even if for a small fraction of objects such inclination may be a slight overestimate. No seeing corrections are attempted for data other than our own.

Uncertainty in the determination of the disk inclination propagates to variables on both axes of the TF diagram. The correction to magnitude for internal extinction increases with increasing inclination angle, while the correction to the observed velocity widths is largest for systems closer to face-on. As ellipses were fitted to each galaxy image, we estimated errors in the determination

of e for our data, which include not only the cluster galaxies listed in Table 2 but also a larger field sample of late-type spirals. In figure 13, we display the errors ϵ_e , as derived from our data, plotted versus e . A trend is discernible in the sense that ϵ_e increases with decreasing e . The solid line superimposed on the data

$$\text{med } \epsilon_e = 0.090 - 0.12e + 0.037e^2 \quad (4)$$

yields an estimate of the expected (median) error associated with the ellipticity. We can use eqn. (4) in the computation of the error ϵ_e for sources of data other than ours, for which values of the ellipticity or axial ratio are given without an indication of the associated error.

The distribution of inclination errors shows considerable skewness and kurtosis, especially for low values of the inclination. This combined effect can arise from isophotal maps strongly affected by the light of a bar, the presence of an undetected warp, or other disk distortions.

5. Velocity Widths

The velocity widths have been obtained at several different telescopes, using both radio and optical long-slit techniques. All the radio spectra have been reduced within the same system. Techniques and algorithms applied in the reduction of our data, as well as comparisons with other data sets are described elsewhere (Haynes *et al.* 1997). Here we are mainly concerned with the details related with the characterization of the velocity-width error budget.

5.1. Corrections Applied to 21 cm Velocity Widths

Our 21 cm velocity widths were measured using an algorithm that fits the rising sides of the galaxian profile with low order polynomials and obtains the width at a 50% level of each of the profile horn peaks or single peak, depending on the line shape. Similar techniques have been applied in data drawn from other sources, and we have applied each of the standard techniques to our data as well, and derived recursion relations to convert widths from other sources to our standard. In order to derive a measure of the disk maximum rotational velocity from the observed 21 cm profile width, a number of corrections need to be applied.

First, the broadening effects produced by the instrumental characteristics, the signal-to-noise ratio (S/N) of the spectrum and any smoothing that may have been applied in order to improve the (S/N) need to be accounted for. These broadening processes depend on the shape of the spectral line, i.e. the steepness of the “horns”.

Second, both turbulent and ordered motions contribute to the profile width. We assume that ordered motions are fully produced by rotation, and attempt no corrections related to large scale

phenomena such as warps of the disk, noncircular orbits and motions perpendicular to the disk plane. We statistically correct only for the contributions of turbulent motions.

Third, the observed profile is broadened in the measure $(1 + z)$, where z is the redshift of the source, by relativistic effects.

Fourth, the Doppler observations refer to the line of sight projections of the gas motions. The amplitude of ordered motions occurring in the plane of the disk can be obtained from the observed values when the inclination angle i , between the normal to the plane of the disk and the line of sight, is known.

The *corrected* velocity width will then be

$$W_c = \left[\left(\frac{W_{obs,21} - \Delta_s}{1 + z} \right)^2 - \Delta_t^2 \right]^{1/2} \frac{1}{\sin i} \quad (5)$$

where $W_{obs,21}$ is the observed 21 cm width and Δ_s is the correction for the effects of instrumental broadening and of any smoothing applied in the reduction stage. The latter term also takes into account the distortions that result with varying (S/N) and a dependence on the observed shape of the line profile. The term Δ_t accounts for the broadening produced by turbulent motions, and the factor $1/\sin i$ deprojects the disk.

5.2. The Velocity Width Error Budget

Each one of the correction steps adds a measure of uncertainty to the determination of the velocity width, which needs to be carefully tracked since, as we shall see, they constitute one of the principal contributions to scatter in the TF diagram.

Let the measurement of the spectrum yield a width $W_{obs,21}$, with an associated error on the measurement $\epsilon_{w,obs}$.

Based on our own numerical simulations, we assume that the uncertainty associated with the quantities Δ_s and Δ_t is approximately 25% of the value of each, i.e. $\epsilon_s = 0.25\Delta_s$, and $\epsilon_t = 0.25\Delta_t$.

The uncertainty on $1/\sin i$, the inclination correction, depends principally on the accuracy with which the disk ellipticity has been measured. The dependence of ϵ_e on e is shown in Figure 13 and parametrized by eqn. (4). The error on the measurement of e propagates to that in $1/\sin i$ via

$$\epsilon_i^2 = \left[\frac{d(1/\sin i)}{d(e)} \right]^2 \epsilon_e^2 \quad (6)$$

where we have neglected the effect of the uncertainty on the value of q_o .

The uncertainty ϵ_w associated with W_c is then

$$\epsilon_w^2 = \frac{\epsilon_{w,obs}^2 + \epsilon_s^2}{(1+z)^2 \sin^2 i} + \frac{\epsilon_t^2}{\sin^2 i} + \epsilon_i^2 W_c^2 \sin^2 i \quad (7)$$

The relative error on the width, ϵ_w/W_c , increases with decreasing inclination, because the first two terms in eqn. (7) are proportional to $1/\sin^2 i$ and because $\epsilon_i \sin i$ increases as the disk gets closer to face-on, as shown in Figure 13. Similarly, ϵ_w/W_c increases with decreasing W_c , because $\epsilon_{w,obs}$, ϵ_s and ϵ_t are to the first order independent of width, and therefore constitute an increasingly large fraction of the width as W_c decreases. This is shown in Figure 14.

The relative importance of the various terms contributing to ϵ_w does of course depend on the inclination of the system. For highly inclined systems, the uncertainty on i does not play a very important role, while for systems with $i < 65^\circ$, the term in ϵ_i can be the most important. The terms in ϵ_s and ϵ_t seldom account for more than a quarter of the total error budget, and more often they account for less than 10% ; in addition, in most cases in which these terms account for more than 10% of the width error, the latter is usually quite small in absolute terms. Thus, the simplicity of our approximation of ϵ_s and ϵ_t as constant fractions of the corrections Δ_s and Δ_t , respectively, is well justified; a more elaborate parametrization of ϵ_s and ϵ_t is unnecessary.

5.3. Corrections applied to Optical Velocity Widths

For a sizable fraction of objects in our sample, we use velocity widths obtained from optical, single slit spectroscopy. For these objects, adequate 21cm line profiles are generally unavailable. A comparison of optical and radio widths, and a detailed discussion of the derivation and treatment of both quantities is given elsewhere (Haynes *et al.* 1997).

A number of corrections need to be applied to optical velocity widths; some are similar to those applied to radio widths and described above, others are not, such as those responding to the *ad hoc* requisite that the corrected widths be compatible with those obtained via radio means.

First we apply an additive offset Δ_{sh} to the observed or reported optical width, $W_{obs,opt}$, such that this correction will make it equivalent to the radio width, corrected for instrumental, smoothing and signal-to-noise broadening effects. Such offset depends principally on the adopted measuring technique and on the shape of the rotation curve, as discussed in Haynes *et al.* (1997). Because the HI widths tend to sample regions of disks that generally extend beyond the edge of the regions sampled by optical rotation curves, the offset between the two widths depends on the extent over which the spectrum spatially maps the disk, and on whether the rotation curve is seen to be still rising, flat, or falling at the outer parts of the disk sampled by the spectrum. In a reanalysis of the optical rotation curve data of MFB, Persic and Salucci (1996) have adopted a velocity width measurement that corresponds to the value of the rotational speed at a radius R_{opt}

within which 80% of the disk’s I band light is enclosed. We also adopt here that criterion. For objects for which both optical rotation curve and 21 cm line data are available, the corrected 21 cm width and the optical width measured at R_{opt} provide a good match. For galaxies where the sampling of the optical spectrum does not reach as far out as R_{opt} , we extrapolate the rotation curve, using the parametrized “universal rotation curve” form of Persic and Salucci (1991), as described in detail in Haynes *et al.* (1997). A second offset correction would be necessary, in order to account for poor estimates of the position angle (PA) of disks’ major axes. This should always be an additive term, because any misestimate of the PA will generally reduce the measured width. An estimate of the error incurred in estimating the PA is difficult. We have simulated the effects of errors on the observed width by misalignment of the spectrograph slit, both in PA and in centering, and have found that the errors remain negligible for $PA < 15^\circ$ or so. Given the uncertainty in estimating the PA error, we chose not to apply a correction for this effect. Any net mean offset would be small, and would be incorporated in the Δ_{sh} term.

Next, a $(1+z)^{-1}$ relativistic correction and an inclination correction are applied, as described for the radio widths in the preceding section. The corrected width derived from optical rotation curves is then

$$W_c = \frac{W_{obs,opt} - \Delta_{sh}}{(1+z) \sin i}, \quad (8)$$

and the resulting uncertainty associated with W_c is

$$\epsilon_w^2 = \frac{\epsilon_{w,obs}^2 + \epsilon_{sh}^2}{(1+z)^2 \sin^2 i} + \epsilon_i^2 W_c^2 \sin^2 i \quad (9)$$

where $\epsilon_{w,obs}$ is the measurement uncertainty on $W_{obs,opt}$, ϵ_{sh} is the uncertainty on the shape dependent offset correction Δ_{sh} , the amplitude of which is very sensitive on whether $W_{obs,opt}$ is obtained from the rotation curve by interpolating between observed values or extrapolating beyond the last measured radius; ϵ_i is the uncertainty on $(1/\sin i)$, as shown in the preceding section. For the widths derived from the data of MFB, we have inferred uncertainties $\epsilon_{w,obs}$ from the tabulation of folded and kinematically recentered rotation curves by Persic and Salucci (1996). When we use data from sources other than ours, for which $\epsilon_{w,obs}$ is not reported and for which a more informed estimate of the width error is not possible, we assume $\epsilon_{w,obs} = 20 \text{ km s}^{-1}$, an error typical for galaxies with measured errors.

6. I band Fluxes and Related Errors

For all the objects used in this study, magnitudes derived from I band CCD images are available. In some cases, other photometric parameters, such as scale lengths and isophotal sizes, are also available. When scale lengths are measured, it is possible to infer an asymptotic

magnitude, which results from extrapolating the “curve of growth” of isophotal magnitudes to infinity, assuming that the surface brightness falls exponentially with the measured scale length. Such extrapolation is applied to the magnitude measured at an isophotal level between 23.5 and 24.0 mag arcsec^{−1} (which is found at a distance of 4 scale lengths from the center of the galaxy), and it amounts typically to a few hundreds of a magnitude. We adopt such an asymptotal measure as our estimate of the I band flux.

There is a significant offset in the mean values of the total uncorrected magnitude, between our own observations and those from the other main source utilized in this paper, i.e. those by MFB. We compare 217 galaxies for which both MFB and our magnitudes are available. Of those, 196 have magnitude differences smaller than 0.3 magnitudes; galaxies with magnitude discrepancies larger than 0.3 mag are not used further in comparing the two scales. The 196 galaxies yield a mean difference in the measured total magnitude of $\langle m_{our} - m_{MFB} \rangle = -0.053$. This difference does however exhibit a systematic trend, in the sense that the difference becomes larger (more negative) for objects of brighter apparent magnitude. We tentatively attribute part of the effect to the fact that some of the observations of MFB of objects of relatively large angular size were carried out with a relatively small chip on the 1m telescope at Siding Spring; sky subtraction may have been less effective than for the larger objects observed with that system. We apply a correction to the MFB magnitude scale as follows:

$$m_{MFB}^{cor} = m_{MFB} - 0.08 - 0.016\delta + 0.011\delta^2 \quad (10)$$

for objects of $m_{MFB} < 13.6$, where $\delta = m_{MFB} - 10$, and $m_{MFB}^{cor} = m_{MFB}$ for $m_{MFB} \geq 13.6$.

The overlap of objects between our and the HM samples (51) and that between the HM and MFB samples (86) are too small to yield a statistically significant offset between scales. We thus use the raw HM magnitudes unchanged. The scatter in the comparisons gives an idea of the reliability of I band magnitudes. While comparisons of repeat observations within a given data set report consistency to within 0.04 mag, comparison between different data sets suggests that the quality of the data may be slightly worse, on the order of 0.06–0.07 mag. Large discrepancies, in excess of 0.15 mag, occur more frequently than would be expected if errors were random; these cases probably arise from the occasional misjudgement of photometric conditions, or from misidentification of the source. In the tabulation of data utilized for this study, we footnote large discrepancies between different data sources. When several sources are available, we generally adopt average values, else we justify our choice in the notes to Table 2.

Adopted raw magnitudes are corrected first for extinction within our Galaxy, by adopting the Burstein and Heiles (1978) tabulation of B-band extinctions, converted to I-band by means of $A_I = 0.45A_B$, and by a cosmological k-term, adopted from Han (1992): $k_I = 0.16z$. The internal extinction in each galaxy’s disk is treated in the manner described in paper II. All magnitudes are converted to a face-on perspective, by applying an additive term which depends on both the inclination of the system to the line of sight and on its intrinsic luminosity. The corrected apparent

magnitude is then

$$m_c = m_{obs} - A_I + k_I - \Delta m_i \quad (11)$$

where m_{obs} is the raw asymptotic magnitude and Δm_i the internal extinction correction. m_{obs} , A_I , k_I , Δm_i are positive quantities. The internal extinction correction was parametrized in paper II as

$$\Delta m_i = -\gamma \log(1 - e) = \gamma \log(a/b) \quad (12)$$

where e is the corrected ellipticity and the parameter γ depends on absolute luminosity of the galaxy as shown in Figure 7c of paper II ($\gamma = 0.5$ for $M_I > -19$, $\gamma = 1.0$ for $-20.3 > M_I > -22$, and γ changes linearly by -0.4 mag^{-1} elsewhere).

For application in a TF program, however, it is convenient to have the value of γ parametrized as a function of velocity width. In Figure 15, we plot the magnitude residuals with respect to a direct fit to the template TF relation of the cluster sample, which we will obtain in Paper VII. The data plotted pertain to the all sky spiral sample described in Papers I and II (filled circles) and the cluster sample (unfilled squares). The magnitude residuals are computed after correcting the magnitudes by imposing $\Delta m_i = 0$ in eqn. (11), and separately for five different ranges of velocity widths; since residuals are plotted versus $\log(a/b)$, their trends mimic the internal extinction correction that should be applicable.

The solid lines inset on panels (c) through (e) are not fits to the data points but rather the mean internal extinction laws that would apply to the subset of galaxies, according to the model of eqn. (12) derived for late-type spirals (the slope of the line is the value of γ which would be used, according to the precepts of paper II, averaged over all the galaxies in the subset). We adopt those lines as our internal extinction laws. For the fastest rotators the internal extinction appears to increase slowly for values of $\log(a/b)$ smaller than about 0.5, then more steeply at higher inclinations. The apparent bilinearity of the internal extinction law may be related to a decrease of scale height to scale length ratio with overall galaxy size, or to a decreasing degree of clumpiness of opaque regions in the disk with increasing disk size: both effects would shift the inclinations at which internal extinction increases more steeply to values closer to edge-on. The departure of the data from the simple model of eqn. (12) is significant enough, especially for objects of intermediate inclination in panel (a) of Figure 15, that the adoption of an alternative model is warranted. In order to keep it simple, for the fastest rotators we adopt a bilinear model, which involves two different values of γ , respectively for high and low values of $\log(a/b)$. The adopted values of γ , tabulated for different values of velocity width, are given in Table 3; for the two bins of higher width, two values of γ are given, meant to apply respectively below and above the value $\log(a/b) = 0.52$. Table 3 is used in the estimate of the internal extinction correction that leads to the values listed in col (14) of Table 2. Finally, for objects with $i = 90^\circ$, an additional

0.05 mag internal extinction term is adopted. Higher extinction occurring in edge-on systems is to be expected from extinction models, and visually dramatized by the effect of dust lanes bisecting disks; it is also statistically suggestive in our data, which includes 31 objects listed at $i = 90^\circ$. A correction of only 0.05 mag over the inclination dependent law may be conservative, but it is likely that a significant fraction of the systems deemed to be at $i = 90^\circ$ are not exactly edge-on (the determined value of i being highly sensitivity on the assumed value of q_0 , see eqn 2), and additional 0.05 mag of extinction is a fair statistical correction which averages over such systems.

The cluster sample contains a sizable fraction of galaxies of type earlier than Sbc, for which all our extinction relations had been obtained. On the grounds of suggestive statistical evidence, based on the comparison of about 30 galaxies earlier than Sab and about 160 galaxies of type Sb with the galaxies of later types, we adopt for all galaxies of type earlier than Sbc an extinction relation which, at any given inclination, is 85% of that estimated for the Sbc and Sc galaxies as shown in Figure 15 and Table 3. This “differential treatment”, which is typically smaller than the total error on the magnitude, as discussed below, has a negligible impact on the final template obtained in paper VII. While it needs to be corroborated by the study of larger samples, the sense of the correction appears clear, and it points in the direction of an increasing ratio between scale heights of the dust and of the stellar population sampled by the I band, towards later types.

Estimates of the accuracy of our tabulated magnitudes derive from the addition in quadrature of two main quantities. One is the measurement error, resulting from estimates of the photometric conditions at the time of data taking, the quality of the sky subtraction, the effects of neighboring interfering objects in the frame, the quality of the asymptotic extrapolation of the light profile, etc. In general, these sources of errors are not itemized in the literature. Whenever an estimate of this error is not given in the sources used other than our own, we assume a value of 0.04 mag. If more than one independent measurement of the magnitude is available for a given object, we adopt as a measurement error either 0.04 mag or one half of the magnitude difference between extreme values, whichever is largest. The second source of error derives from the corrections expressed by eqn. (11), of which Δm_i is usually the most important. We adopt an uncertainty of 15% on the value of γ and propagate the error, together with that on the uncertainty on the axial ratio, to that on the estimate of the extinction correction. This component of the uncertainty typically exceeds the measurement error, for inclinations larger than about 60° . In paper VII, we shall refer to the combination in quadrature of measurement and processing errors described above as the “total measurement error” on the magnitude.

7. Global Characteristics of the Cluster Sample

Here we investigate the global properties of the cluster galaxies listed in Table 2. As discussed in section 3, for each cluster, two principal subsamples have been defined: one of objects believed to be cluster members (**in**) and a second (**in+**) that, in addition to cluster members, also includes objects in the periphery and near the systemic velocity of the cluster, but sufficiently removed

(extending to about 3 or 4 Abell radii) that a membership assignment cannot be confidently made.

The distribution of apparent I band magnitudes of all galaxies in the **in+** samples is shown in Figure 16. It illustrates that for this sample no assumption of completeness to any useful flux limit can be made. Similarly, Figure 17 displays the distribution of isophotal radii of the same galaxies, as measured at $\mu_I = 23.5 \text{ mag arcsec}^{-2}$, demonstrating a similar unsuitability of the data to be usefully analyzed with criteria applicable to angular size limited samples.

Many haphazard circumstances affect the construction of a cluster TF sample, which eventually lead to distributions such as those in Figures 16 and 17: inaccuracy of parameters listed in catalogs from which samples are extracted, a priori availability of redshifts, telescope scheduling, weather conditions, a posteriori sifting by final data quality, availability of data from external sources based on different selection criteria, etc. The analysis of the data requires that corrections be applied, that take into consideration the peculiarities of the sample selection. Unfortunately, individual cluster samples are still small enough that sacrifice of a fraction of available objects made to obtain a clean subset of simple completeness characteristics, and to which straightforward corrections can be applied, is painfully impractical. In order to maintain sample integrity and overcome the effects of selection biases, we believe the best current approach is that of estimating corrections via computer simulations with artificial samples that reproduce the completeness characteristics of the data.

An analysis of the completeness characteristics of a larger sample of spirals, which includes the current cluster sample as a subset, is presented in Papers I and II. In Paper II, we used visibility functions of luminosity and central disk surface brightness to illustrate built-in biases in the optical catalogs from which the observed objects were extracted.

In Figure 18, we show the distribution of absolute magnitudes of all the galaxies included in the **in+** cluster samples. The line superimposed onto the histogram represents our best estimate of the spiral galaxy luminosity function (LF) from which the observed sample may be assumed to have been extracted. The latter is parametrized by a Schechter formula with $M^* + 5 \log h = -21.6$ and $\alpha = -0.50$, obtained by a match between the observed distribution in each cluster with the luminosity functions of spiral galaxies derived by Sandage, Binggeli and Tammann (1984) in their survey of the Virgo cluster. The skewness of the adopted LF departs from the nearly gaussian luminosity function of normal spirals found in the Las Campanas survey of Sandage *et al.* (1984). This is due to a small contribution of Sdm systems which contaminates the “normal” spiral sample. Objects fainter than $M_I \simeq -19$ are only observed in the nearby clusters/groups, such as Fornax, Eridanus, Ursa Major and MDL59. For comparison, the Milky Way galaxy has an approximate I band absolute magnitude of -22, M31 of -22.5 and M33 of -19.7 (Pierce and Tully 1992). The average color (B-I) of spirals such as those in our sample is about 1.5 mag. The shape of the LF from which cluster samples are extracted is important in the computation of incompleteness bias corrections. In Paper VII we carry out those computations for two values of α , including the one quoted above, in order to ascertain the sensitivity of the correction on the

characteristics of the adopted LF.

8. Membership Assignment

Cluster membership was assigned according to criteria that varied somewhat from cluster to cluster, depending on how well the cluster parameters are known. In clusters for which a large body of redshift information is available, and for which reliable estimates of the velocity dispersion and caustic curves are known, membership assignment has been extended with some confidence to larger distances from the cluster center. On the other hand, for less well defined clusters, a more conservative approach has been adopted: membership was restricted to objects projected more closely to the cluster center and/or with velocities closer to its systemic velocity.

In some cases, clusters are located at small angular and velocity separations from nearby aggregates, such as in the case of the NGC 383 and NGC 507 groups, Fornax and Eridanus, A2197 and A2199, A2634 and A2666. In each case, assignment to the **in** and **in+** samples was made according to criteria of angular and velocity separation, similar to those extensively described in the study of the A2634/A2666 system by Scodeggio *et al.* (1995). In some cases, galaxies in cluster peripheries may with nearly equal likelihood be considered peripheral members of either of two nearby clusters; we have then avoided entry duplication, assigning each galaxy to only one cluster listing. A discussion of choices for individual cases follow.

NGC 383 and NGC 507 Groups. The centers of the two groups are separated by 3.4° and are virtually at the same redshift (Sakai *et al.* 1994). The two clusters have often been lumped into a single unit referred to as the “Pisces cluster”, although Sakai *et al.* are able to clearly separate their binary nature. As a visual separation criterion one can adopt the line of $RA = 01^h 10^m$. There is no ambiguity in the membership assignment to any objects projected inside the circle of $1 R_A$ radius. Three galaxies projected between the circles of $1 R_A$ and $2 R_A$, UGC 764, UGC 810 and UGC 820, are assigned to NGC 507, although they are nearly equidistant to the center of the NGC 383 group. A percolation algorithm assigns them to NGC 507, which appears to be the more conspicuous of the two groups. An effect of the proximity of the two groups is that the peripheral members listed in the NGC 383 table are preferentially to the West of the cluster center. A262 is located approximately 7° to the NE of the center of NGC 507, bounding the group to the east.

Fornax and Eridanus. Eridanus is a group about 14° to the North of the well developed Fornax cluster. It is listed as group G31 by de Vaucouleurs (1975), and its center is often associated with the location of the S0 galaxy NGC 1332. An appraisal of the distribution of galaxies in the region does however suggest that this loose aggregate is organized around several high ranked but well separated galaxies. We have adopted as the center a position intermediate between the locations of the bright galaxies NGC 1325, NGC 1332, NGC 1353, NGC 1359, NGC 1395 and NGC 1407, i.e. $RA = 03^h 30^m$, $Dec = -21^\circ 30'$. The distribution of redshifts of 148 galaxies with $cz < 3000 \text{ km s}^{-1}$, within 13° from that center and North of $Dec = -28^\circ$ (a boundary chosen in

order to avoid confusion with Fornax), looks fairly regular and centered near $V_{cmb} = 1530 \text{ km s}^{-1}$, which is very close to the central velocity adopted by MFB of 1534 km s^{-1} . There is no overlap of the areas enclosed within the respective $1 R_A$ circles of each cluster. Galaxies 416-G6, 416-G20 and 486-G5, which are roughly equidistant from the centers of both Fornax and Eridanus and at about $2R_A$ from each, are assigned as peripheral members (**in+** sample) to Fornax; this decision does not affect their location in the TF diagram, as distances are assigned to them on the basis of their individual redshifts, rather than that of either cluster.

Cancer. The structure of this cluster has been studied in detail by Bothun *et al.* (1983), who identified several groups, named A through E, spread in velocity over 2800 km s^{-1} . In Table 2 we have assigned membership to each group according to the criteria of Bothun *et al.*, and label as cluster members those objects pertaining to the largest of the groups, group A. In Figure 5, members of the foreground group D are identified by unfilled triangles, while members of background groups B and C are identified by unfilled squares. For all galaxies, angular distances from the cluster center, θ , are referred to the center of group A.

A1367. Membership assignment to A1367 has been extended to about 4° from the center, well in excess of $2 R_A$, because the cluster structure is well defined by a rich redshift data base, there are no confusing nearby clusters or groups, and caustic curves have been reliably determined by Regös and Geller (1989). We interpolate their set of caustic curves to obtain those corresponding to a value of the density parameter $\Omega_o = 0.3$, and use the latter to define cluster membership.

Centaurus. Lucey *et al.* (1986) give a detailed analysis of the structure of the Centaurus cluster and are able to separate two main components, both centered at the same sky location but with redshifts differing by about 1500 km s^{-1} . The two clumps are known as Cen30 and Cen45. In Figure 8, galaxies assigned to Cen45 are identified by unfilled squares, while those assigned to the more conspicuous Cen30 cluster are identified by filled circles. The separation between the two groups, on a galaxy per galaxy basis, is tenuous. Some of the objects assigned to Cen45 on the basis of their radial velocity may be “redshift outliers” of Cen 30. This case is more likely for 322-G48 and 323-G42; in trying to keep the Cen30 sample as free of contamination as possible we have conservatively included them in Cen45. Since only 6 galaxies are assigned membership to Cen45, and because of the uncertainties in the assignment, we deem incautious an estimate of the mean distance of Cen45 using such a sparse and uncertain sample. We notice that in the periphery of the cluster, at $\theta > 3^\circ$, the mean redshift of galaxies with known redshift is perhaps 160 km s^{-1} larger than the systemic velocity adopted for Cen30 (as derived by Lucey *et al.*). Given the difficulty in separating Cen30 and Cen45, the possibility can be suggested that the true velocity of Cen30 may be slightly higher than estimated by Lucey *et al.* and adopted here. This unusually large uncertainty on the systemic velocity of the cluster should be folded in any estimate of the uncertainty of its peculiar velocity.

It should be noted that the Centaurus region lies at very low galactic latitude, and the

corrections for extinction arising in the Milky Way are important, occasionally exceeding 0.3 mags. Because galactic extinction is quite patchy, those corrections can be rather uncertain, especially when their amplitude is large. This accounts for the significantly larger magnitude corrections in this region, and may be an important source of the large scatter in the TF diagram for this cluster (see Paper VII).

Coma (A1656). A situation similar to that discussed for A1367 is encountered here. The cluster has been very well studied and reliable caustic curves have been published by Regös and Geller (1989). We extend membership $2R_A$, to galaxies beyond included within the $\Omega_o = 0.3$ caustic curves, out to a maximum radial distance of $\theta = 4^\circ$. This is possible because the cluster structure is well sampled and no confusing clumps appear projected on it. The substructure reported in West *et al.* (1995, and refs. therein) in Coma is all enclosed within the inner 1 R_A of the cluster, and does not raise concerns regarding membership assignment for the spiral population.

A2197/A2199. The two clusters are separated by less than 1.5° and 200 km s^{-1} , respectively on the sky and in systemic velocity. Separation of the two clusters on a galaxy per galaxy basis, outside the central cores, is uncertain. Nonetheless, the mistaken assignment of a galaxy to one cluster rather than the other in the binary system would produce an error in the estimated magnitude of less than 0.05 mag, comparable with the uncertainty that derives from our measurement and inclination corrections. The two galaxies for which membership assignment is most doubtful are 260930 and 260561, which have been tentatively assigned to A2197; 250561 is not used in TF fits, however, because of its low disk inclination of 37° . The impact of cluster membership concerns is thus relatively minor in this region.

Pavo I and Pavo II. These are two rather poorly defined, sparse groups with a comparatively small number of available redshifts. We have obtained approximate center coordinates and systemic velocities using the available redshift data base. In doing so, we have set an arbitrary boundary between the domains of the two groups as follows: Pavo I is at $Dec < -68^\circ$ for $19^h < RA < 19.8^h$, and $Dec < -65^\circ$ for $RA > 19.8^h$. Within that rough division, we identify Pavo I based on 32 redshifts at $cz < 6000 \text{ km s}^{-1}$ and within 5° of $RA = 20^h 13^m$, $Dec = -71^\circ 00'$, to which we assign a systemic velocity of $V_{cmb} = 4104 \text{ km s}^{-1}$. The uncertainty of this determination is no better than 100 km s^{-1} . For comparison, note that MFB assume a systemic velocity of $V_{cmb} = 3518 \text{ km s}^{-1}$. For Pavo II the data base is better; using 90 redshifts with $cz < 6000 \text{ km s}^{-1}$ and within 5° of $RA = 18^h 42^m$, $Dec = -63^\circ 20'$, we assign to Pavo II a systemic velocity $V_{cmb} = 4470 \text{ km s}^{-1}$, with an uncertainty on the order of 70 km s^{-1} and a velocity dispersion of about 450 km s^{-1} . For comparison, Bell and Whitmore (1989) obtain a systemic velocity of 4437 km s^{-1} and a velocity dispersion of 507 km s^{-1} , based on 42 redshifts. MFB distinguish between Pavo II and DC1842–63, assigning $V_{cmb} = 4712$ to DC1842–63 and $V_{cmb} = 4357$ to Pavo II, which they identify with a sparse component centered roughly on DC1842–63. Abell, Corwin and Olowin (1989) identify Pavo II with S0805. In Figure 10, solid and unfilled circles identify our best estimate of members and peripheral members of Pavo I, while filled and unfilled squares do

so for Pavo II.

A2634/A2666. This region has been well studied recently by Pinkney *et al.* (1993) and Scodeggio *et al.* (1995). We follow the membership assignment criteria of the latter. A2634 is very well sampled, while A2666 is sufficiently so to allow a good determination of the systemic velocity and of the velocity dispersion, which indicates a significantly less massive character than A2634. Membership assignment to A2634 is extended to 2.5° from the center of A2634; within that distance, however, a foreground subgroup in the A2634 is encountered (A2634-F in Scodeggio *et al.* (1995) at $V_{cmb} = 7182 \text{ km s}^{-1}$; the six galaxies associated with that group in Table 2 are identified by a membership code of “7” and by unfilled squares in Figure 12. Galaxies associated with A2666 are identified by a membership code “6” in table 2. The membership assignment of 476–075 to A2634 is rather marginal; it is just as likely to be a galaxy in the cluster foreground, projected 0.6° from its center. An expanded TF sample and distance analysis for this region is discussed in Scodeggio *et al.* (1996).

9. Summary

We have presented a homogeneous set of data on 782 spiral galaxies localized in the fields of 24 groups or clusters of galaxies, which can be used for the determination of redshift independent distances using the TF technique. The clusters have systemic velocities between about 10^3 and 10^4 km s^{-1} , and range in structural properties from systems that are relatively evolved, such as Coma, to loose aggregates such as the nearby groups Ursa Major and MDL59.

The data include new observations obtained by us and observations by others, available in the public domain. Photometric properties are obtained from CCD images in the I band. Spectroscopic parameters are derived from both single-dish radio observations in the 21 cm line and from long-slit emission line optical spectra.

Particular attention has been given to the assignment of cluster membership. Galaxies have been separated into three main classes: (a) cluster members, which are assumed to be all at the cluster redshift (**in** sample); (b) peripheral cluster members, which are at a redshift very close to that of the cluster but removed from the cluster center by angular separations larger than about 2 Abell radii; jointly with the objects in class (a) they are said to be part of the **in+** sample; (c) interlopers, which include foreground and background objects, and members of peripheral groups, dynamically separate from the main cluster. Three hundred and seventy four galaxies comprise the **in** samples and 584 define the total of the **in+** samples.

We have discussed the characteristics of the errors associated with the parameters of relevance for the TF analysis, in particular the error budget for the velocity widths, which contribute an important source of uncertainty to the TF relation.

These data are used in an accompanying paper (paper VII) to obtain a TF template relation

and to derive the deviations of the individual clusters from smooth Hubble flow.

It is a pleasure to thank Dr. M. S. Roberts for carefully reading this paper, making suggestions that significantly improved it and for being kind enough not to comment on its soporific virtues. The results presented here are based on observations carried out at the Arecibo Observatory, which is part of the National Astronomy and Ionosphere Center (NAIC), at Green Bank, which is part of the National Radio Astronomy Observatory (NRAO), at the Kitt Peak National Observatory (KPNO), the Cerro Tololo Interamerican Observatory (CTIO), the Palomar Observatory (PO), the Observatory of Paris at Nançay and the Michigan–Dartmouth–MIT Observatory (MDM). NAIC is operated by Cornell University, NRAO by Associated Universities, inc., KPNO and CTIO by Associated Universities for Research in Astronomy, all under cooperative agreements with the National Science Foundation. The MDM Observatory was jointly operated by the University of Michigan, Dartmouth College and the Massachusetts Institute of Technology on Kitt Peak mountain, Arizona. The Hale telescope at the PO is operated by the California Institute of Technology under a cooperative agreement with Cornell University and the Jet Propulsion Laboratory. This research was supported by NSF grants AST94–20505 to RG, AST90-14850 and AST90-23450 to MH and AST93–47714 to GW.

REFERENCES

- Aaronson, M. and Mould, J. 1983, ApJ 265, 1
- Aaronson, M., Bothun, G.D., Mould, J., Huchra, J., Schommer, R. and Cornell, M. 1986, ApJ 302, 536
- Aaronson, M., Bothun, G.D., Cornell, M.E., Dawe, J.A., Dickens, R.J., Hall, P.J., Han, M.S., Huchra, J.P., Lucey, J.R., Mould, J.R., Murray, J.D., Schommer, R.E. and Wright, A.E. 1989, ApJ 338, 654
- Abell, G., Corwin, H.G. and Olowin, R.P. 1989, ApJS 70, 1
- Bell, M., and Whitmore, B. 1989, ApJS 70, 139
- Bernstein, G.M., Guhathakurta, P., Raychaudhury, S., Giovanelli, R., Haynes, M.P., Herter, T. and Vogt, N.P. 1994 AJ 107, 1962
- Bothun, G.D., Geller, M.J., Beers, T.C. and Huchra, J.P. 1983, ApJ 268, 47
- Bothun, G.D., Aaronson, M., Schommer, R.E., Mould, J.R., Huchra, J.P. and Sullivan, W. 1985, ApJS 57, 423
- Bottinelli, L. *et al.* 1990, A&AS 82, 391
- Bureau, M., Mould, J.R. and Staveley-Smith, L. 1996, ApJ 463, 60 (BMS)
- Burstein, D. and Heiles, C. 1978, ApJ 225, 40
- da Costa, L.N., Freudling, L.N., Wegner, G., Giovanelli, R., Haynes, M.P. and Salzer, J.J. 1996, ApJ 468, L5 (paper V)
- Davies, J. and Burstein, D. 1995, eds. of *Opacity in Spiral Disks*, Kluwer Academic Publishers, Dordrecht.
- Fontanelli, P. 1984, A&A 138, 85
- Freedman, W.L., Wilson, C. and Madore, B.F. 1991 ApJ 372, 455
- Freudling, W., da Costa, L.N., Wegner, G., Giovanelli, R., Haynes, M.P. and Salzer, J.J. 1995, AJ 110, 920 (Paper III)
- Freudling, W., da Costa, L.N., Wegner, G., Giovanelli, R., Haynes, M.P. and Salzer, J.J. 1995, in Potsdam Workshop, in press
- Gavazzi, G. 1987, ApJ 320, 96
- Giovanelli, R., Haynes, M.P., Salzer, J.J., Wegner, G., da Costa, L.N. and Freudling, W. 1994, AJ 107, 2036 (Paper I)

- Giovanelli, R., Haynes, M.P., Salzer, J.J., Wegner, G., da Costa, L.N. and Freudling, W. 1995, AJ 110, 1059 (Paper II)
- Giovanelli, R., Haynes, M.P., Wegner, G., da Costa, L.N., Freudling, W. and Salzer, J.J. 1996, ApJ 464, L99 (Paper IV)
- Giovanelli, R., Haynes, M.P., Herter, T., Vogt, N.P., da Costa, L.N., Freudling, W., Salzer, J.J. and Wegner, G. 1996b, AJ submitted (Paper VII)
- Giovanelli, R., Haynes, M.P., Chamaraux, P., da Costa, L.N., Freudling, W., Salzer, J.J. and Wegner, G. 1995, in *Examining the Big Bang and Diffuse Background Radiations*, proc. of IAU Symp. nr. 168, ed. by M. Kafatos and Y. Kondo, p. 183, Kluwer:Dordrecht
- Han, M. 1992, ApJS 81, 35
- Han, M. and Mould, J.R. 1992, ApJ 396, 453 (HM)
- Haynes, M.P. *et al.* 1997, in preparation
- Kent, S. and Gunn, J. 1982, AJ 87, 945
- Kogut, A. *et al.* 1993, ApJ 419, 1
- Lauberts, A. 1982, *The ESO/Uppsala Survey of the ESO(B) Atlas* (Garching:ESO)
- Lewis, B.M. 1985, ApJS 59, 161
- Lucey, J.R., Gray, P.M., Carter, D. and Terlevich, R.J. 1991, MNRAS 248, 804
- Lucey, J.R., Currie, M.J. and Dickens, R.J. 1986, MNRAS 222, 427
- Maia, M., da Costa, L.N. and Latham, D. 1989, ApJS 69, 809
- Mathewson, D.S., Ford, V.L. and Buchhorn, M. 1992, ApJS 81, 413 (MFB)
- Nilson, P. 1973, *Uppsala General Catalogue of Galaxies*, Acta Univ. Upsal. Ser. V:A, Vol. 1.
- Persic, M. and Salucci, M. 1991, ApJ 368, 60
- Persic, M. and Salucci, M. 1996, ApJS in press
- Pierce, M. and Tully, R.B. 1988, ApJ 330, 579 (PT88)
- Pierce, M. and Tully, R.B. 1992, ApJ 387, 47
- Pinkney, J., Rhee, G., Burns, J.O., Hill, J.M., Oegerle, W.R., Batuski, D. and Hintzen, P. 1993, ApJ 416, 36
- Regös, E. and Geller, M.J. 1989, AJ 98, 755

- Sakai, S., Giovanelli, R. and Wegner, G. 1994, AJ 108, 33
- Sandage, A., Binggeli and Tammann, G., B. 1984, AJ 90, 1759
- Schneider, S., Thuan, T.X., Magri, C. and Wadiak, J. 1991, ApJS 72, 2455
- Schommer, R. A., Bothun, G.D., Williams, T.B. and Mould, J.R. 1993, AJ 105, 97
- Scodeggio, M. and Gavazzi, G 1993, ApJ 409, 110
- Scodeggio, M., Solanes, J.M., Giovanelli, R. and Haynes, M.P. 1995, ApJ 444, 41
- Scodeggio, M., Giovanelli, R. and Haynes, M.P. 1996, AJin press
- Tully, R.B. and Fisher, J.R. 1977, A&A 54, 661
- Vaucouleurs, G. de 1975, in *Stars and Stellar Systems*, vol. IX, p. 557, ed. by A. Sandage, M. Sandage and J. Kristian, Univ of Chicago Press, Chicago.
- Vaucouleurs, G. de, de Vaucouleurs, A., Corwin, H.G., Paturel, G. and Fouquet, P. 1991, *Third Reference Catalog of Galaxies*, Springer–Verlag, eds.
- West, M.J., Jones, C. and Forman, W. 1995, ApJ 451, L5
- Willmer, C.N.A., Focardi, P., Chan, R., Pellegrini, P.S. and da Costa, L.N. 1991, AJ 101, 57
- Zabludoff, A.I., Huchra, J.P. and Geller, M.J. 1990, ApJS 74, 1
- Zwicky, F. *et al.* 1961–68, *Catalogue of Galaxies and Clusters of Galaxies* I–VI, Cal. Inst. of Tech., Pasadena.

This preprint was prepared with the AAS L^AT_EX macros v4.0.

Fig. 1.— Stereographic distribution of the 24 clusters listed in Table 1, in Cartesian supergalactic coordinates. Labels in the (X, Y) plot identify clusters; label “PP” refers to the three groups in the Perseus–Pisces supercluster, namely N383, N507 and A262; label “GA” refers to the structures in the Great Attractor region, namely Hydra, Cen30, ESO508, Antlia and N3557. Dashed circles have radii of 3000 and 6000 km s^{−1}, respectively.

Fig. 2.— Sky and velocity distribution of galaxies in the groups centered around NGC 383 and NGC 507. Filled circles identify galaxies selected as cluster members (**in** sample), unfilled circles refer to galaxies in the cluster periphery (additional members in the **in+** sample) and asterisks identify foreground and background galaxies. Dots give the location of galaxies with known redshift in the field, but without available peculiar velocity measurement. Dashed lines in each case identify circles of one ($1 R_A$) and two ($2 R_A$) Abell radii; the dotted circle in the NGC 383 plot refers to the $1 R_A$ circle of NGC 507; the dotted circle in the NGC 507 plot refers to the $1 R_A$ circle of NGC 383.

Fig. 3.— Sky and velocity distribution of galaxies in the clusters A262 and A400. Filled circles, unfilled circles, asterisks, dots and dashed circles follow the same convention as in Figure 2.

Fig. 4.— Sky and velocity distribution of galaxies in the clusters Fornax and Eridanus. Filled circles, unfilled circles, asterisks, dots and dashed circles follow the same convention as in Figure 2. Unfilled triangles in the Fornax sky plot identify Eridanus members; unfilled triangles in the Eridanus sky plot identify Fornax members.

Fig. 5.— Sky and velocity distribution of galaxies in the clusters Cancer and Antlia. Filled circles, unfilled circles, asterisks, dots and dashed circles follow the same convention as in Figure 2. In the Cancer plots, unfilled triangles identify objects assigned by Bothun *et al.* (1983) to their “B and C clumps”, while unfilled squares identify galaxies in their “D clump”.

Fig. 6.— Sky and velocity distribution of galaxies in the Hydra cluster (A1060) and in the group around NGC 3557. Filled circles, unfilled circles, asterisks, dots and dashed circles follow the same convention as in Figure 2.

Fig. 7.— Sky and velocity distribution of galaxies in the clusters A1367 and Ursa Major. Filled circles, unfilled circles, asterisks, dots and dashed circles follow the same convention as in Figure 2. Caustics in the lower panel of A1367 are plotted for a value of the cosmological density parameter $\Omega_0 = 0.3$.

Fig. 8.— Sky and velocity distribution of galaxies in the clusters Centaurus (A3526) and Coma (A1656). Filled circles, unfilled circles, asterisks, dots and dashed circles follow the same convention as in Figure 2. We identify the Centaurus (A3526) cluster with the foreground component Cen30 (Lucey *et al.* 1986). Unfilled squares in the Centaurus panels identify galaxies that have been assigned to the background cluster Cen45. Caustics in the lower panel of A1656 are plotted for a value of the cosmological density parameter $\Omega_0 = 0.3$.

Fig. 9.— Sky and velocity distribution of galaxies in the clusters ESO 508 and A3574 (Klemola 27). Filled circles, unfilled circles, asterisks, dots and dashed circles follow the same convention as in Figure 2. The cluster NW of center of A3574 and SE of center of ESO 508 is A1736, a background structure at $z \sim 0.04$. Unfilled squares in the plots of A3574 identify three galaxies in the group S753.

Fig. 10.— Sky and velocity distribution of galaxies in the clusters A2197, A2199, Pavo and Pavo II (S0805). In the A2197/99 plots, filled circles and triangles identify members of A2199 and A2197, respectively. Unfilled circles identify peripheral members of the binary system. Pavo II members are identified by filled squares, while Pavo members are displayed as filled circles; unfilled squares and circles identify peripheral members of, respectively, Pavo II and Pavo. The systemic velocities of A2199 and Pavo II are indicated by horizontal dashed lines, respectively in the two lower panels of the figure.

Fig. 11.— Sky and velocity distribution of galaxies in the clusters MDL59 and Pegasus. Filled circles, unfilled circles, asterisks, dots and dashed circles follow the same convention as in Figure 2.

Fig. 12.— Sky and velocity distribution of galaxies in the clusters A2634 and A2666. Filled circles, unfilled circles, asterisks, dots and dashed circles follow the same convention as in Figure 2. The dotted circle in the A2634 sky plot is the $1 R_A$ circle of A2666; likewise, the dotted circle in the A2666 plot is at $1 R_A$ for A2634. Unfilled squares in the plots of both clusters refer to objects in a group in the foreground of A2634 near $7,000 \text{ km s}^{-1}$; this group is closer to A2634, in projection on the sky, and closer in redshift to A2666. Foreground and background objects are only plotted in the A2634 figures.

Fig. 13.— Distribution of I band ellipticity errors, plotted as a function of the measured ellipticities, for objects with CCD photometry measured by us. Galaxies pertain to the cluster sample presented in this paper and to a field sample of late-type spirals. The solid line represents eqn. (4) in the text, an estimate of the median value of the error, which can be applied to data sets for which ellipticity errors are not reported.

Fig. 14.— Fractional error on the velocity width of 2000 cluster and field spirals, plotted versus the corrected velocity width.

Fig. 15.— Magnitude residuals computed with respect to a TF template relation, obtained in paper VII, computed before the internal extinction correction is applied to the data. Data points refer to running averages for the all sky spiral sample discussed in Papers I and II (filled circles) and for the cluster sample (**In+**) introduced in this paper (unfilled squares). The mean residuals are plotted versus the mean log of the axial ratio (corrected for seeing), an indication of the disks' inclination to the line of sight. Solid lines are *not* fits to the data; they represent instead the internal extinction correction law, eqn. (12), resulting from averaging the value of γ for all the galaxies in subsamples (c) through (e); see text for details on bilinear model for (a) and (b). γ gives the slope of the extinction line. Panels (a) to (e) refer to non-overlapping bins in $\log W_c$, i.e. galaxies with $\log W_c > 2.60$ (a), 2.5 to 2.6 (b), 2.4 to 2.5 (c), 2.3 to 2.4 (d) and $\log W_c < 2.3$ (e).

Fig. 16.— Apparent, raw I band magnitude distribution of all galaxies in the **in+** cluster samples, including cluster members and peripheral objects.

Fig. 17.— Distribution of isophotal angular radii of all galaxies in the **in+** cluster sample, including cluster members and peripheral objects.

Fig. 18.— Absolute I band magnitude distribution of all galaxies in the **in+** cluster sample, including cluster members and peripheral objects. The solid line superimposed on the histogram represents the spiral galaxy luminosity function from which the observed sample is assumed to be extracted, parametrized by a Schechter formula with $M_I^* + 5 \log h = -21.6$ and $\alpha = -0.50$.

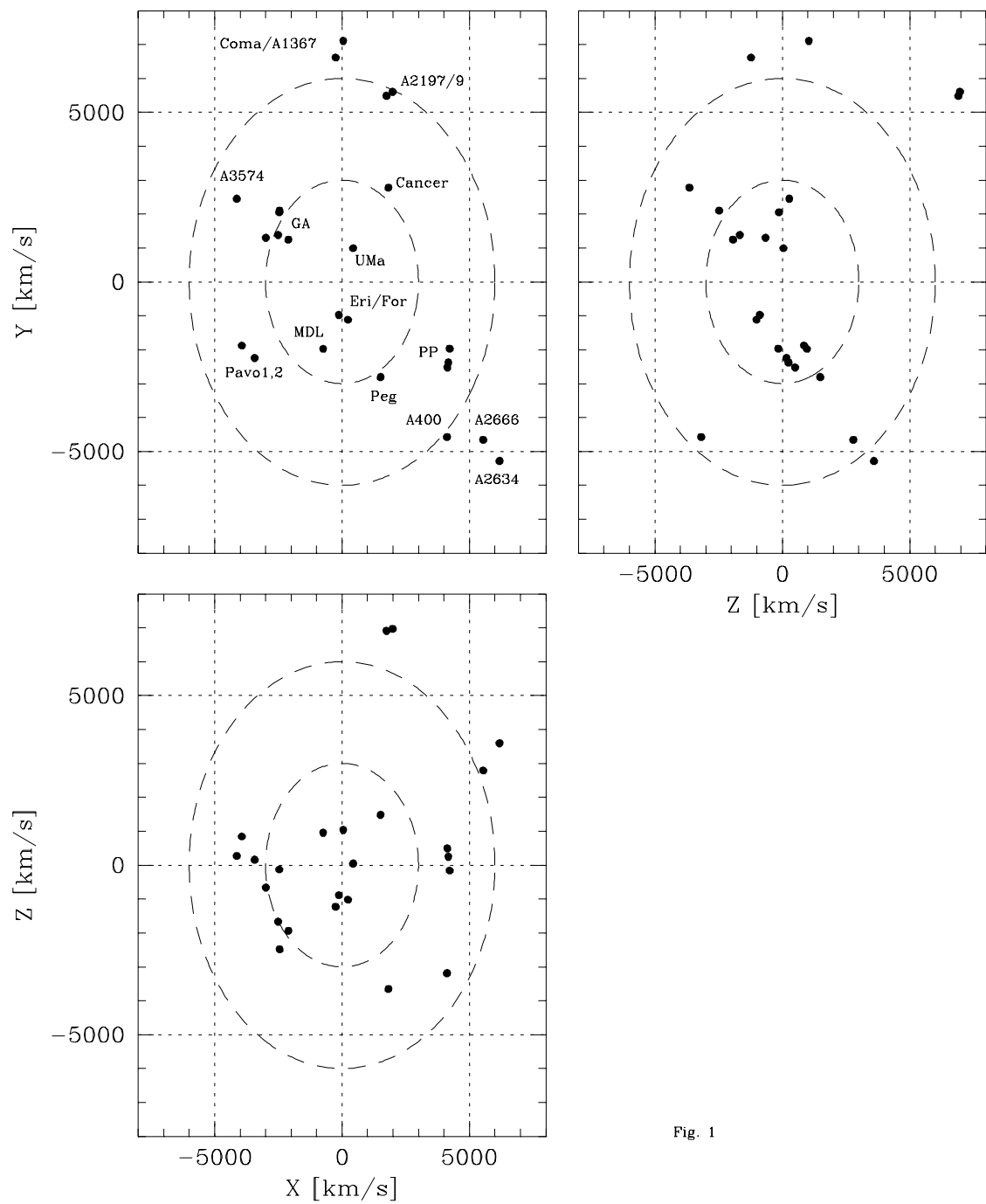


Fig. 1

TABLE 1
CLUSTERS USED IN TEMPLATE

Cluster	R.A. hhmmss.s	Decl. ddmmss	V_{hel} km s ⁻¹	V_{cmb} km s ⁻¹	SGL °	SGB °	X km s ⁻¹	Y km s ⁻¹	Z km s ⁻¹	Ref
NGC 383	010430.0	+321200	5161(32)	4865	-31.4	5.9	4130	-2524	496	1
NGC 507	012000.0	+330400	5091(99)	4808	-29.7	2.9	4172	-2380	247	1
A 262	014950.0	+355440	4918(80)	4664	-25.0	-2.0	4220	-1970	-159	1
A 400	025500.0	+055000	7142(75)	6934	-48.0	-27.4	4123	-4574	-3187	2
Eridanus	033000.0	-213000	1665(30)	1534	281.7	-41.8	230	-1117	-1020	
Fornax	033634.0	-353642	1415(45)	1321	262.5	-42.1	-127	-972	-885	
Cancer	081730.0	+211400	4705(80)	4939	56.7	-47.7	1824	2781	-3651	3
Antlia	102745.0	-350411	2800(100)	3120	149.4	-38.4	-2104	1246	-1937	
A 1060 = Hydra	103427.7	-271626	3733(50)	4075	139.4	-37.5	-2452	2104	-2483	
NGC 3557	110735.0	-371600	3000(60)	3318	151.1	-30.2	-2511	1386	-1668	
A 1367	114154.0	+200700	6408(88)	6735	92.2	-10.5	-254	6617	-1228	2
Ursa Major	115400.0	+485300	896(40)	1101	66.3	2.4	437	994	46	4
A 3526 = Cen30	124606.0	-410200	3041(150)	3322	156.4	-11.4	-2987	1302	-659	5
A 1656 = Coma	125724.0	+281500	6917(68)	7185	89.6	8.3	48	7109	1041	2,6
ESO508	130954.0	-230854	2900(100)	3210	140.1	-2.3	-2462	2055	-128	
A 3574 = Klemola 27	134606.0	-300900	4548(11)	4817	149.3	3.2	-4134	2455	273	7
A 2197	162630.0	+410100	9138(100)	9162	70.5	49.5	1982	5609	6968	2
A 2199	162654.0	+393800	8970(98)	8996	72.4	50.2	1741	5487	6913	2
S 805 = Pavo II	184200.0	-632000	4470(70)	4444	205.5	11.0	-3936	-1878	847	8
Pavo	201300.0	-710000	4100(100)	4055	213.1	2.3	-3433	-2242	162	
MDL59	220018.0	-321400	2590(75)	2317	249.4	24.4	-742	-1976	957	9
Pegasus	231742.6	+075557	3888(80)	3519	-61.7	24.9	1514	-2809	1483	
A 2634	233554.9	+264419	9240(79)	8895	-40.5	23.8	6187	-5283	3596	10
A 2666	234824.0	+264824	8118(81)	7776	-40.1	21.1	5537	-4658	2790	10

REFERENCES.—(1) Sakai *et al.* 1994; (2) Zabludoff, Huchra & Geller 1990; (3) Bothun *et al.* 1983; (4) Pierce and Tully 1988; (5) Lucey *et al.*; (6) Kent and Gunn 1982; (7) Willmer *et al.* 1991; (8) Bell and Whitmore 1989 and additional redshifts; (9) Maia *et al.* 1989; (10) Scodeggio *et al.* 1995.

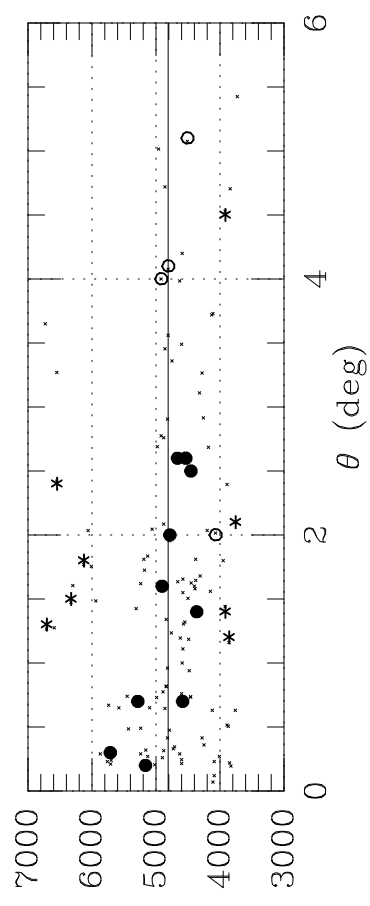
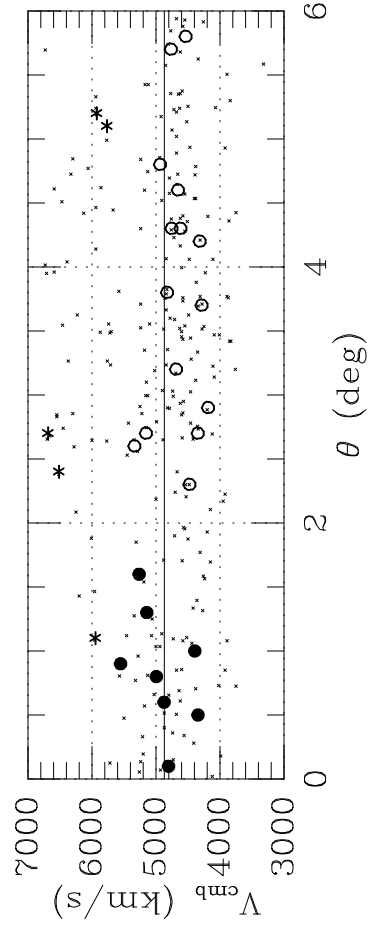
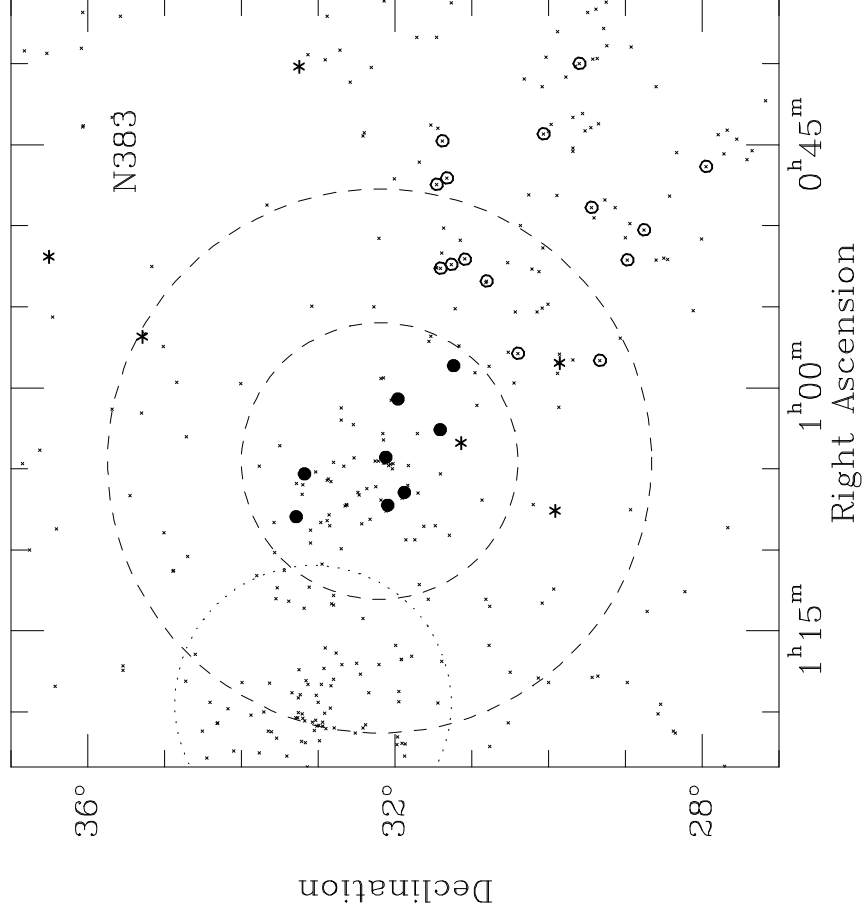


fig. 2

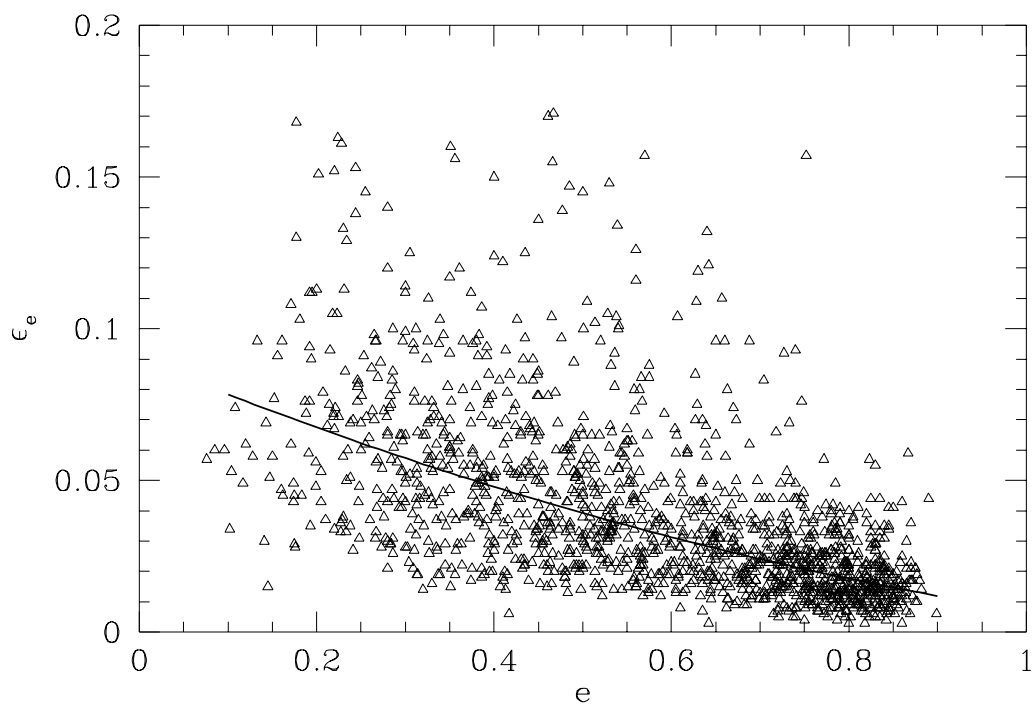


Fig. 13

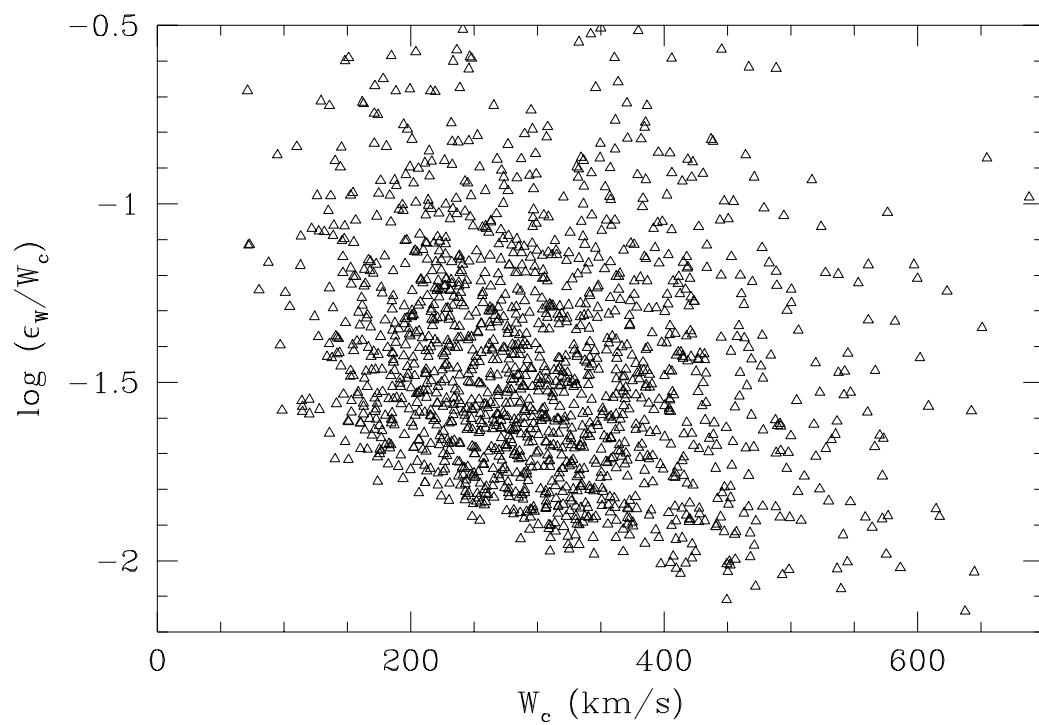


Fig. 14

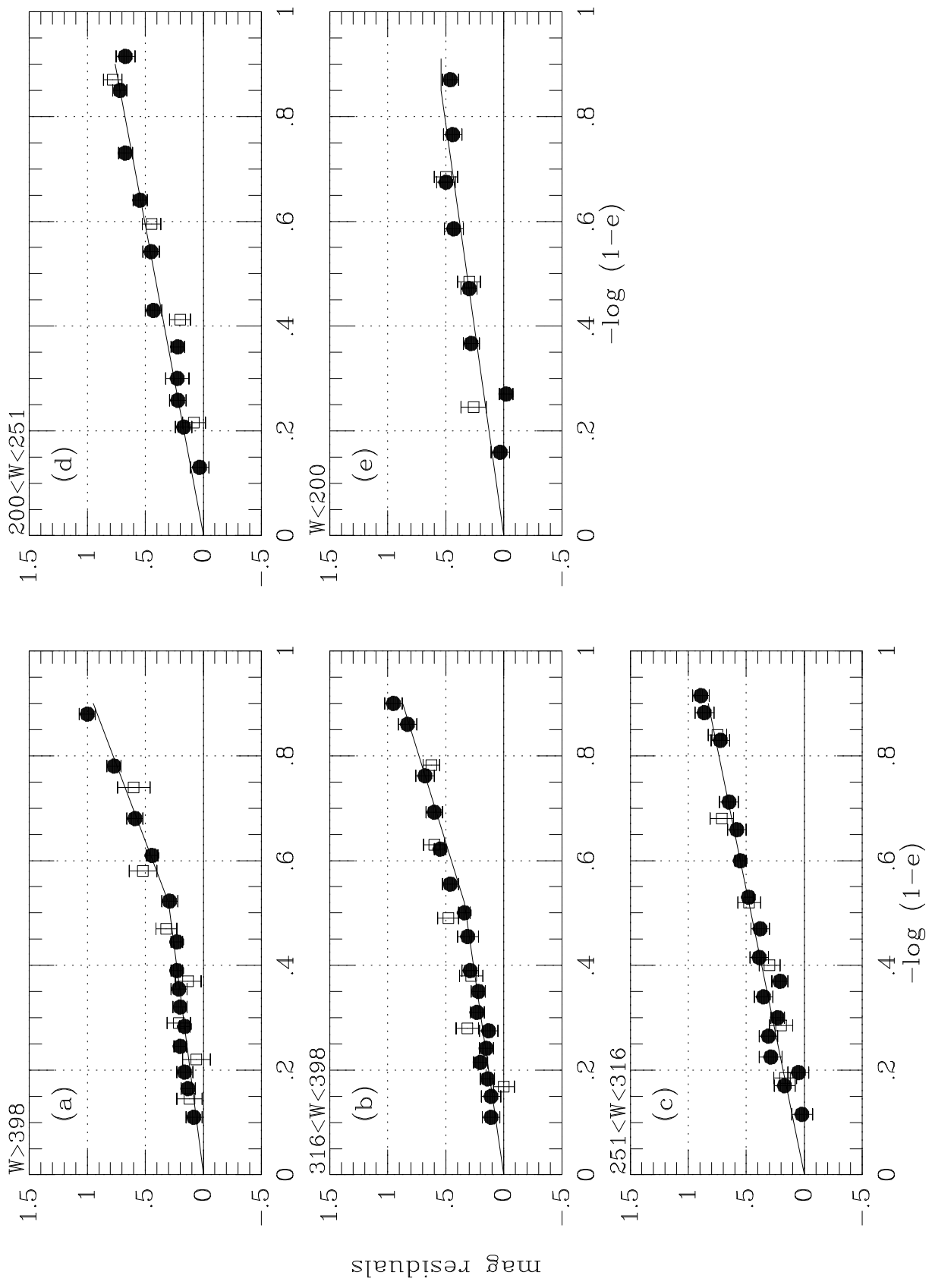


Fig 15

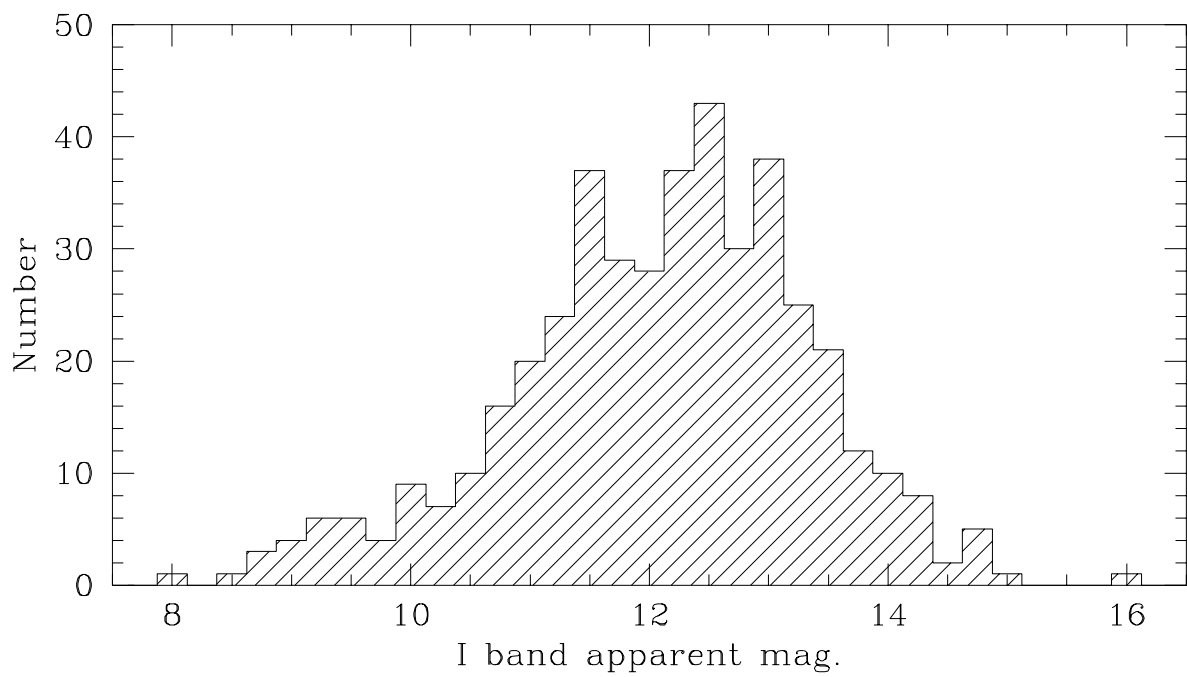


Fig. 16

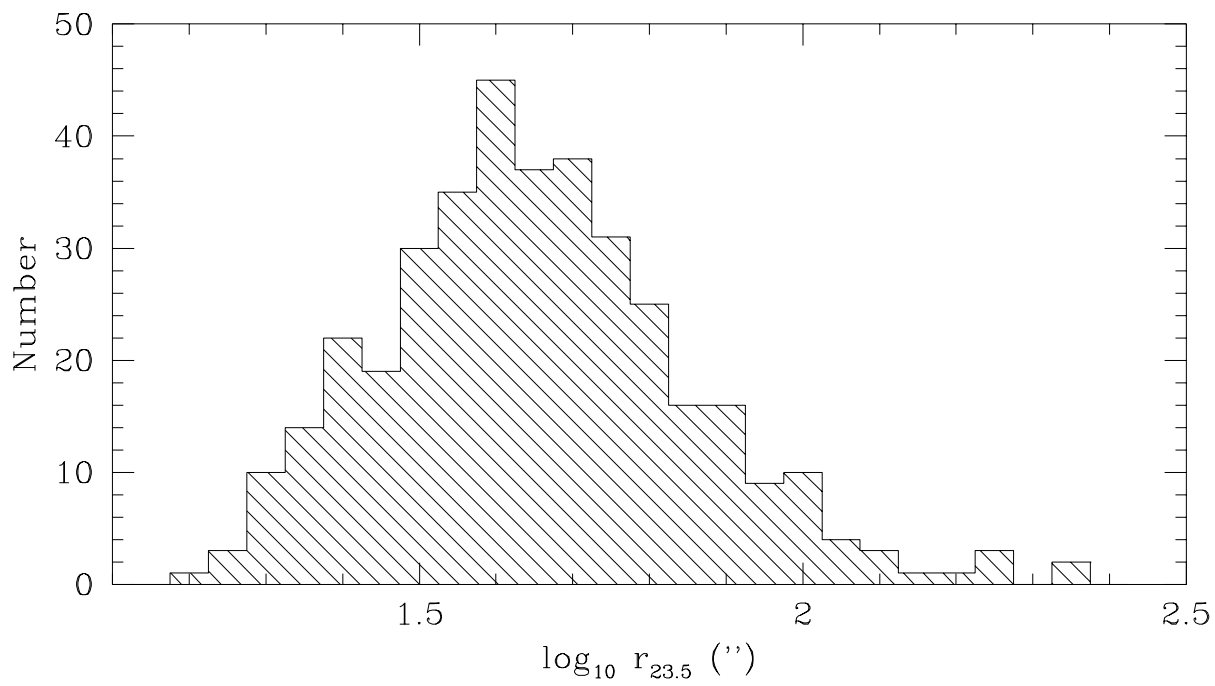


fig. 17

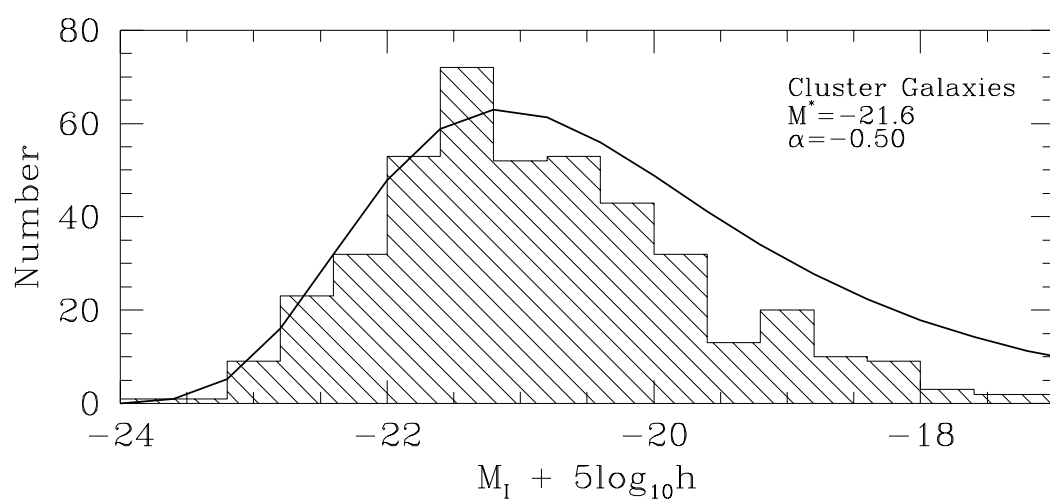


fig. 18

TABLE 2
GALAXY PARAMETERS, BY CLUSTER

Names	R.A. <i>h m s</i>	Dec. <i>d m s</i>	T	V_{cmb} <i>km s⁻¹</i>	θ <i>°</i>	Mem	W –	W_1 <i>km s⁻¹</i>	W_{cor} –	i <i>°</i>	log W_{cor}	m	m_{cor}	M_{cor}	Notes
(1)	(2)	(3)	(4)	(5)	(6)	(7)	(8)	(9)	(10)	(11)	(12)	(13)	(14)	(15)	(16)
NGC 383 Group															
U00453	003959.5	+293600	5	4544	5.8	g	186	164	167	78	2.224(11)	15.02	14.51	-18.79(15)	a 0 *
U00457/500-075	004011.2	+331453	4	5927	5.2	b	289	256	262	78	2.418(22)	13.77	13.10	-20.79(10)	a 0
U00485/501-012	004420.9	+300357	5	4935	4.8	g	354	330	330	90	2.519(05)	12.74	11.69	-21.79(17)	a 0
100561/500-095	004446.3	+312253	4	4762	4.3	g	176	153	194	52	2.288(65)	14.39	14.13	-19.28(15)	a 0 *
U00501/501-021	004621.0	+275647	5	4769	5.7	g	384	357	358	85	2.554(09)	12.98	12.14	-21.27(16)	a 0
U00509	004704.0	+311940	5	4825	3.8	g	212	187	204	66	2.310(14)	14.15	13.75	-19.69(09)	a 0
U00511/501-023	004727.7	+312733	5	4287	3.7	g	277	253	258	80	2.411(10)	13.92	13.22	-19.95(11)	a 0
U00525/501-028	004853.0	+292633	3	4621	4.3	g	225	196	225	60	2.352(20)	13.43	13.14	-20.20(10)	h 0
U00540/501-031	005016.0	+284540	3	4661	4.6	g	264	238	284	57	2.452(18)	12.97	12.69	-20.67(10)	h 0
U00549/520-002	005156.2	+363017	5	5769	5.1	b	237	212	214	81	2.331(17)	14.51	13.86	-19.97(14)	a 0
U00557/501-041	005203.5	+310538	3	4192	2.9	g	266	240	261	67	2.416(24)	13.62	13.25	-19.87(09)	h 0 *
U00556/501-040	005208.0	+285829	3	4318	4.2	g	366	342	391	61	2.592(31)	12.99	12.76	-20.43(10)	h 0 *
U00562/N295	005224.6	+311615	3B	5163	2.7	g	470	442	472	69	2.674(08)	11.36	11.08	-22.51(13)	h 0
U00565/N296	005238.1	+312424	5	5340	2.6	g	247	217	225	75	2.352(21)	13.75	13.18	-20.48(08)	a 0 *
U00575/501-048	005326.3	+304817	4	4346	2.7	g	285	253	254	84	2.404(12)	13.82	13.04	-20.17(17)	x 0 *
U00614/520-006	005650.4	+351729	5B	2064	3.5	f	202	180	213	58	2.327(24)	12.76	12.48	-19.10(08)	a 0
U00624/N338	005752.3	+302358	2	4479	2.3	g	526	500	529	71	2.724(07)	11.47	11.18	-22.09(08)	a 0
U00629/501-062	005819.0	+291953	5	4689	3.2	g	189	165	308	32	2.489(73)	13.51	13.35	-20.02(05)	a 0 *
U00632/501-063	005827.9	+295143	2B	6691	2.7	b	400	353	394	64	2.595(22)	12.77	12.50	-21.66(08)	a 0 *
U00633/501-065	005837.6	+311420	3	5272	1.6	c	394	364	370	80	2.568(15)	12.98	12.54	-20.92(15)	x 0 *
U00646/501-071	010040.9	+315800	3B	4999	0.8	c	378	340	358	72	2.554(10)	12.50	12.18	-21.27(08)	a 0
U00669/501-075	010234.2	+312453	5	5556	0.9	c	280	244	247	81	2.393(16)	13.28	12.59	-20.87(16)	a 0
U00673/501-079	010324.5	+310820	5	5952	1.1	b	283	258	274	70	2.438(08)	14.06	13.56	-20.33(21)	x 0 *
U00679	010418.0	+320726	10	4813	0.1	c	187	156	156	90	2.194(20)	14.99	14.34	-19.12(13)	h 0
U00697/501-093	010518.5	+331100	3B	4402	1.0	c	324	282	299	71	2.476(36)	12.78	12.42	-21.03(26)	a 0 *
U00714/501-103	010627.9	+315303	5	4345	0.5	c	221	194	269	46	2.431(31)	12.75	12.53	-20.93(07)	a 0
U00724/501-111	010713.5	+320610	2	4880	0.6	c	321	297	448	41	2.651(35)	12.32	12.19	-21.27(05)	a 0 *
110090/501-113	010736.0	+295500	3	6522	2.4	b	232	206	239	59	2.379(19)	14.38	14.07	-20.03(05)	a 0 *
U00732/501-116	010757.2	+331723	5	5147	1.3	c	267	239	291	55	2.463(18)	12.77	12.49	-20.96(04)	a 0
NGC 507 Group															
U00764	011024.5	+344153	5	4455	2.5	c	213	187	187	86	2.272(15)	15.26	14.57	-18.86(16)	a 0
U00800/502-012	011234.0	+281333	5	4513	5.1	g	169	144	239	37	2.378(78)	13.73	13.59	-19.70(06)	a 0 *
U00809/520-033	011300.0	+333300	5	3920	1.4	f	314	289	291	83	2.464(09)	13.55	12.74	-20.25(15)	x 0 *

TABLE 3
INTERNAL EXTINCTION

$\log W$	γ
2.05	0.57
2.15	0.60
2.25	0.68
2.35	0.84
2.45	0.92
2.55	0.65, 1.40 *
2.65	0.58, 1.70 *

*Change of slope at
 $-\log(1 - \epsilon) = 0.52$.